



Shahid Chamran  
University of Ahvaz

# Journal of Applied and Computational Mechanics



Research Paper

## The Flow of Jeffrey Nanofluid through Cone-Disk Gap for Thermal Applications using Artificial Neural Networks

Abeer S. Alnahdi<sup>1</sup>, Zeeshan Khan<sup>2</sup>, Taza Gul<sup>3,4</sup>, Hijaz Ahmad<sup>5,6,7,8</sup>

<sup>1</sup> Department of Mathematics and Statistics, Faculty of Science, Imam Mohammad Ibn Saud Islamic University (IMSIU), Riyadh, 11432, Saudi Arabia, Email: asalnahdi@imamu.edu.sa

<sup>2</sup> Department of Mathematics, Abdul Wali Khan University Mardan, 23200, Khyber Pakhtunkhwa, Pakistan, Email: zk70964@gmail.com

<sup>3</sup> Department of Mathematics, City University of Science and Information Technology, Peshawar, 25000, Pakistan, Email: tazagul@cusit.edu.pk

<sup>4</sup> DoST-Directorate General of Science and Technology, Khyber Pakhtunkhwa, Peshawar, 25000, Pakistan, Email: tazagul.dost@kp.gov.pk

<sup>5</sup> Department of Mathematics, Faculty of Science, Islamic University of Madinah, Madinah, Saudi Arabia

<sup>6</sup> Near East University, Operational Research Center in Healthcare, Nicosia, PC: 99138, TRNC Mersin 10, Turkey, Email: hijaz.ahmad@neu.edu.tr

<sup>7</sup> Department of Computer Science and Mathematics, Lebanese American University, Beirut, Lebanon

<sup>8</sup> Department of Mathematics and Informatics, Azerbaijan University, Jeyhun Hajibeyli street, 71, AZ1007, Baku, Azerbaijan

Received November 15 2023; Revised March 18 2024; Accepted for publication March 19 2024.

Corresponding author: T. Gul (tazagul@cusit.edu.pk)

© 2024 Published by Shahid Chamran University of Ahvaz

**Abstract.** This study investigates the flow of Jeffrey nanofluid through the gap between a disk and a cone, incorporating the influences of thermophoresis and Brownian motion within the flow system. Suitable variables have used to convert the modeled equations to dimension-free notations. This set of dimensionless equations has then solved by using Levenberg Marquardt Scheme through Neural Network Algorithm (LMS-NNA). In this study, it has been observed that the absolute error (AE) between the reference and target data consistently falls in the range  $10^{-4}$  to  $10^{-5}$  demonstrating the exceptional accuracy performance of LMS-NNA. In all four scenarios it has noticed that transverse velocity distribution has declined with augmentation in magnetic and Jeffery fluid factors by keeping all the other parameters as fixed. It is evident that the optimal validation performance  $2.8227 \times 10^{-9}$  has been achieved at epoch 1000 for the transverse velocity when cone and disk gyrating in opposite directions.

**Keywords:** Cone and disk devices; Jeffrey fluid flow; Artificial neural network; Boungiorno model; Heat transfer analysis.

### 1. Introduction

The cone and disk system demonstrates extensive practical and technical utility across various domains. Its applications include finely controlling fluid distribution using conical diffusers, accurately measuring viscosity with viscometers, and act significantly in the development of cutting-edge medical procedures, as extensively detailed in reference [1]. Examining heat in the gap created by a cone and a disk is of utmost importance due to its intricate nature and broad relevance spanning multiple engineering and scientific disciplines, as highlighted in Ref [2]. Shaikholeslami [3] utilized hybrid nanoparticles in the computational analysis of a solar system equipped with an innovative tabulator. Turkyilmazoglu [4] investigated the fluid flow through disk and cone by taking two scenarios namely; static cone moving disk and moving disk static cone and has proved that the optimal cooling performance of the geometry is attained when the disk is in a rotating state while the cone remains stationary, under the condition that the wall temperatures are meticulously maintained at uniform levels throughout. Srilatha et al. [5] analyzed mass and thermal transportations for the flow of fluid in above stated geometry using the thermophoretic motion of particles. Moatimid et al. [6] discussed the nanofluid flow through disk-cone gap and observed that the rotational factors are observed to lead to a reduction in radial velocity and heat flow. The heat transfer for fluid flow amid cone and disk involves the exchange of thermal energy between the fluid and the surfaces of the disk and cone [7]. Shaikholeslami [8] investigated computationally concentrated solar photovoltaic structure with MWCNTs nanoparticles suspended in paraffin. Mandal et al. [9] discussed bio-convective nanofluid flow with impacts of microorganisms and activated energy and have noticed that with a slight change in bio-convective Brownian number there is a huge decline in Nusselt number (almost 96% reduction in it has observed).

Jeffrey fluid is a type non-Newtonian fluid that exhibits viscoelastic properties, implying that their response to shear stress is nonlinear and can be impacted by element like the rate of deformation. Jeffrey fluids are frequently utilized to model complex fluid behaviors in various scientific and engineering applications. In the realm of Jeffrey fluid flow, the fluid's behavior is elucidated using the Jeffrey fluid model, a mathematical framework that considers the fluid's shear-thinning and viscoelastic characteristics [10]. This model typically incorporates parameters defining the fluid's viscosity and elasticity. Researchers and engineers delve into Jeffrey fluid flow in diverse fields, and it serves as a valuable tool for gaining comprehensions in the behavior of fluids that differ from the simple linear relationship amid strain and stress exhibited by Newtonian fluids like oil or water [11-12].



13]. Agarwal et al. [14] inspected computationally the MHD Jeffery fluid flow on an elongating sheet with micro-rotational and thermally radiative effects and highlighted that flow panels have diminished and thermal distribution has escalated with progression in Jeffery and porosity factors. Benal et al. [15] discussed MHD Jeffery fluid flow in a permeable medium on an expanding surface and perceived that velocity panels have amplified with progression in the Jeffery factor. Heat transfer in Jeffery fluid flow refers to the process of thermal energy transfer within a flow of Jeffrey fluids, which are non-Newtonian fluids demonstrating elastic and viscous features under deformation [16, 17]. Heat transfer in Jeffrey fluids has applications in various fields, including polymer processing, biomedical engineering (studying blood flow), and industrial processes where non-Newtonian fluids are involved [18].

Artificial Neural Networks (ANNs) represent a significant breakthrough in artificial intelligence, demonstrating remarkable adaptability in acquiring knowledge from both internal and external data flow during the learning process [19]. In engineering applications, the use of ANNs for predicting fluid flow holds promise and efficiency [20]. ANNs have proven their capability to capture intricate nonlinear relationships within fluid flow data, making them valuable tools for modeling and forecasting fluid behavior. Through training on extensive datasets encompassing flow parameters, boundary conditions, and corresponding fluid flow patterns, ANNs develop the ability to approximate the underlying principles governing fluid dynamics. In the ANN architecture, the input layer receives various flow variables like velocity, pressure, and temperature, while hidden layers extract meaningful features and correlations [21]. The strength of ANNs lies in their capacity to generalize and provide accurate predictions even with limited or noisy data. To enhance the accuracy and robustness of ANN models, a careful selection of network architectures, activation functions, and optimization algorithms is conducted during the design phase. Moreover, integrating domain expertise and combining ANNs with physics-based models can further improve the network's performance. This adaptability positions ANNs as promising tools for addressing a wide range of fluid flow scenarios, making them valuable for design optimization, flow control, and real-time flow prediction in practical engineering applications [22]. Samanta and Mondal [23] developed a predictive model by using ANN and the bivariate spectral quasi-linearization method. This model is designed for the analysis of compressible turbulent boundary-layer flow over a smooth flat surface. Among various approaches, the Levenberg-Marquardt supervised neural networks algorithm (LMS-NNA) stands out as an advanced optimization technique used for training ANNs. It combines principles from the Levenberg-Marquardt (LM) algorithm and backpropagation to efficiently update the network's weights during training. The primary objective of LMS-NNA is to diminish error between the neural network's anticipated outcomes and the actual target values within a supervised learning framework. Mishea and Mondal [24] have used ANN to compute the solution for nanofluid flow with engine oil as base fluid and nanoparticles of  $ZrO_2$ ,  $Fe_3O_4$  and have noted that ANN is the best approach for prediction of drag friction and Nusselt number. ANNs offer a powerful and efficient method for examining the intricate interplay of electromagnetically influenced and chemically reactive fluid flow around an elongated cylinder [25]. ANNs can be leveraged to model and predict complex flow patterns, temperature distributions, and species concentrations near the stretching cylinder [26]. For instance, Aljohani et al. [27] utilized backpropagation LMS-NNA (ANN) to compute coating wire system behavior in the context of Sisko fluid flow on a sheet. Similarly, Sulaiman et al. [28] investigated thermal transport behavior in fluid flow over a surface through supervised neural network techniques.

The relation between fluid dynamics and particle behavior becomes more complex when considering fluid flow influenced by Brownian motion and thermophoresis [29]. Brownian motion introduces unpredictable thermal fluctuations, leading suspended particles to undergo erratic movements within the fluid. These movements have the potential to enhance particle dispersion and diffusion, impacting processes like mixing and particle transport. On the contrary, thermophoresis results from temperature gradients in the fluid, causing particles to migrate from higher to lower temperature regions. This phenomenon significantly affects particle distribution and concentration in a fluid, particularly in applications involving heat transfer or combustion. When combined, Brownian motion and thermophoresis contribute to intricate interactions between particles and fluid, playing crucial roles in various fields such as aerosol science, colloid chemistry, and nanotechnology. In these domains, precise control of particle behavior within a fluid is essential for comprehending and optimizing processes and applications [30-31]. Magodora et al. [32] examined computationally the nanofluid flow with gold-nanoparticles on a spinning disc with impacts of activation energy and observed that with escalation in activation energy there has been an augmentation in concentration panels while a reduction in thermal distribution. Shaikholeslami [33] used a novel numerical scheme for analysis of nanoparticles flow with influence of magnetic effects on a permeable sheet and has detected that Bejan number has augmented with growth in conduction. Almakki et al. [34] examined production of entropy and effects of dissipation on dual diffusive nanofluid flow on gyrating spherical surface. Shaikholeslami [35] examined computationally MHD  $Al_2O_3/H_2O$  nanofluid flow on porous surface. The author of this work has used an innovative technique to evaluate the modeled problem. Brownian motion, driven by thermal fluctuations, leads to the haphazard motion of mixed particles within the fluid, contributing to enhanced heat transfer due to increased convective mixing. Additionally, thermophoresis, induced by temperature gradients, causes particles to migrate within the fluid, altering the local temperature distribution. This migration can influence heat transfer by affecting the concentration and distribution of particles. Falicita et al. [36] discussed Williamson nanofluid flow with impacts of slip constraints, thermophoresis, convection, and Brownian motion. Ibrahim et al. [37] studied the impact of thermophoresis and Brownian motion on fluid flow on an extending sheet with heat generation and chemical reactivity. Almeida et al. [38] examined micro-rotational MHD fluid flow in association with thermophoresis and Brownian motion through a channel.

The literature review revealed that there has been no prior discussion on the flow of Jeffrey fluid through the gap of a disk cone, and that is the main novelty in current investigation. What sets this research apart further is the incorporation of cutting-edge machine-based neuro-computation techniques. By leveraging advanced computational methodologies, our study aims to transcend the limitations of traditional approaches, enhancing the robustness and uniqueness of our findings. This state-of-the-art technique not only elevate the sophistication of the analysis but also provide a more nuanced understanding of the complex collaborations within the Jeffrey fluid flow in the disk cone gap. Brownian motion and thermophoresis phenomena have used to regulate the thermal characteristics of the flow system. In this work the Jeffrey nanofluid flow is considered through the gap of disk and cone with different impacts. Four different scenarios have used in this work for both cone and disk rotation. Suitable variables have used to convert the modeled equations to dimension free notations. This set of dimensionless equations has then solved by using Artificial Neural Networks (ANNs). For this, initially HAM technique has used for evaluation of modeled equations and then to analyze the dynamics of flow Levenberg Marquardt Scheme through Neural Network Algorithm (LMS-NNA) has employed. A specific potential application of the current study in real-world engineering and industry could be in the design and optimization of advanced thermal management systems. The insights gained from this study could be applied to enhance the efficiency of cooling systems in electronic devices, such as microprocessors, where the control and understanding of nanofluid flow characteristics play a crucial role in preserving optimum temperatures. The use of artificial neural networks in this context could contribute to the development of more intelligent and adaptive cooling solutions for electronic components, improving overall performance and reliability.



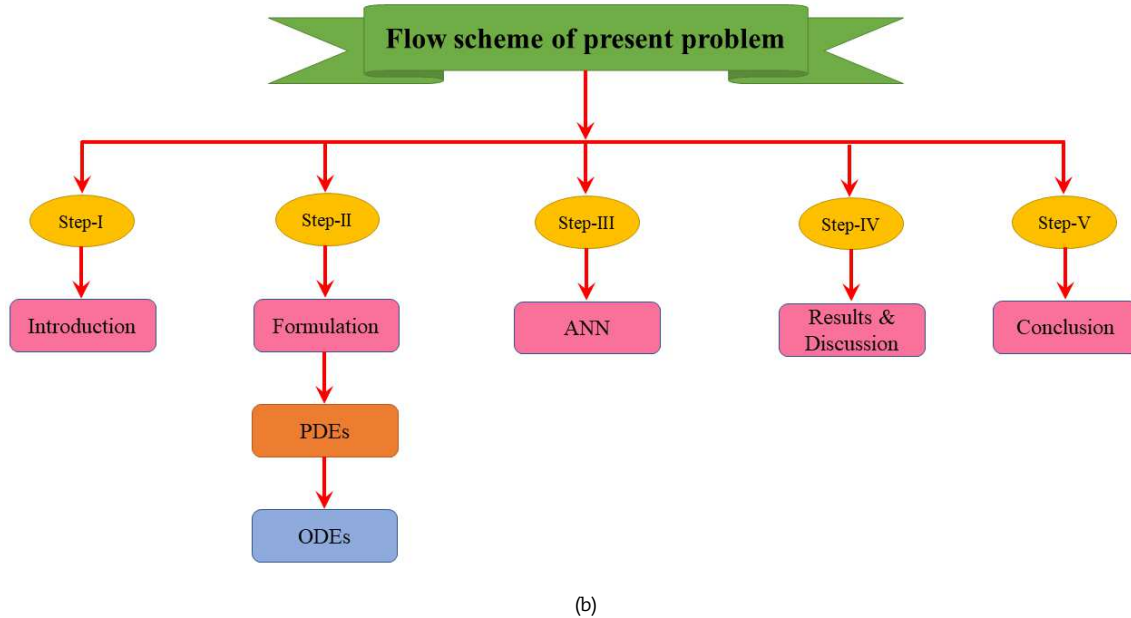
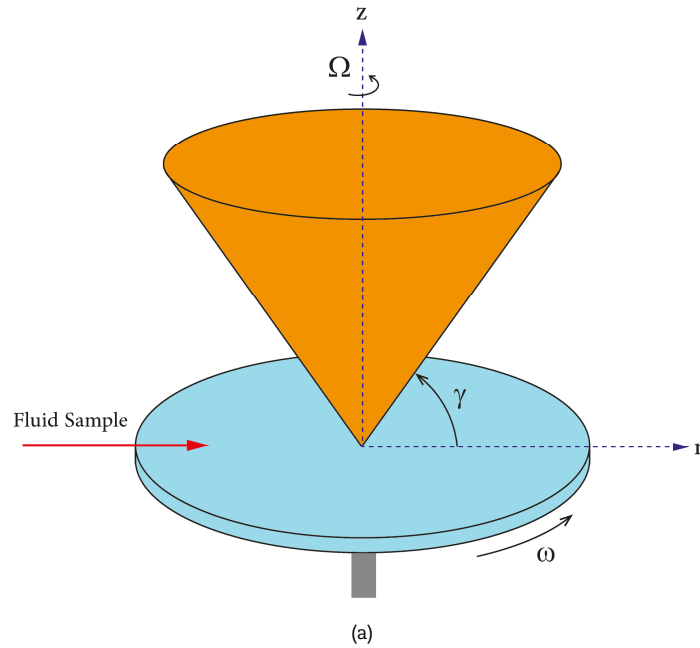


Fig. 1. (a) Geometric configuration of the flow problem, (b) the flow chart.

## 2. Problem Formulation

Take Jeffrey's fluid flow within the gap of disk-cone apparatus, where these devices are oriented at an angle  $\gamma$  to each other. Brownian motion and thermophoresis phenomena are employed to control the thermal characteristics of the flow system. The disk is located at  $z = 0$  and is rotating at an angular velocity  $\omega$  perpendicularly. Simultaneously, the cone is gyrating at an angular flow  $\Omega$  in axial direction, as illustrated in Fig. 1(a). Figure 1(b) is the flow chart of the problem. Here  $(r, \theta, z)$  are selected as coordinates of flow. The flow is investigated under four distinct scenarios regarding the rotations of the disk-cone apparatus.

By incorporating all of the aforementioned assumptions, we have [4, 5, 39- 41]:

$$\frac{1}{r} \frac{\partial(ru)}{\partial r} + \frac{\partial w}{\partial z} = 0, \tag{1}$$

$$u \frac{\partial u}{\partial r} + w \frac{\partial u}{\partial z} - \frac{v^2}{r} + \frac{\partial p}{\partial r} = \frac{v}{1 + \lambda_1} \left( \frac{\partial^2 u}{\partial z^2} - \frac{u}{r^2} + \frac{1}{r} \frac{\partial}{\partial r} \left( r \frac{\partial u}{\partial r} \right) \right) - \frac{\lambda^*}{1 + \lambda} \left( 2u \frac{\partial^3 u}{\partial r^3} + 2w \frac{\partial^3 u}{\partial z \partial r^2} + 2 \frac{\partial u}{\partial r} \frac{\partial^2 u}{\partial r^2} + 2 \frac{\partial^2 u}{\partial z \partial r} \frac{\partial w}{\partial r} - 2 \frac{\partial u}{\partial z} \frac{w}{r^2} - 2 \frac{\partial u}{\partial r} \frac{u}{r^2} - 2 \frac{u^2}{r^3} \right. \tag{2}$$

$$\left. + \frac{\partial^2 w}{\partial r^2} \frac{\partial u}{\partial z} + \frac{\partial^2 w}{\partial r \partial z} \frac{\partial w}{\partial z} + 2u \frac{\partial^3 u}{\partial z^2 \partial r} + 2w \frac{\partial^3 w}{\partial z^3} + \frac{\partial u}{\partial z} \frac{\partial^2 u}{\partial z \partial r} + \frac{\partial w}{\partial z} \frac{\partial^2 u}{\partial z^2} \right),$$



$$u \frac{\partial v}{\partial r} + w \frac{\partial v}{\partial z} + \frac{uv}{r} = \frac{v}{1 + \lambda_1} \left( \frac{\partial^2 v}{\partial z^2} - \frac{v}{r^2} + \frac{1}{r} \frac{\partial}{\partial r} (r \frac{\partial v}{\partial r}) \right) - \frac{\lambda^*}{1 + \lambda} \left( 2u \frac{\partial^3 v}{\partial r^3} + 2w \frac{\partial^3 v}{\partial z \partial r^2} - \frac{\partial v}{\partial z} \frac{w}{r^2} + \frac{\partial^2 v}{\partial r^2} \frac{\partial u}{\partial r} + \frac{\partial w}{\partial r} \frac{\partial^2 v}{\partial z \partial r} - \frac{1}{r} \frac{\partial u}{\partial r} \frac{\partial v}{\partial r} + \frac{v}{r^2} \frac{\partial u}{\partial r} - 2 \frac{uv}{r^3} - \frac{1}{r} \frac{\partial v}{\partial z} \frac{\partial w}{\partial r} + 2u \frac{\partial^2 v}{\partial z^2 \partial r} + 2w \frac{\partial^2 v}{\partial z^3} + \frac{\partial u}{\partial z} \frac{\partial^2 v}{\partial z \partial r} + \frac{\partial w}{\partial z} \frac{\partial^2 v}{\partial z^2} \right), \tag{3}$$

$$u \frac{\partial w}{\partial r} + w \frac{\partial w}{\partial z} = -\frac{\partial p}{\partial z} + \frac{v}{1 + \lambda_1} \left( \frac{\partial^2 w}{\partial z^2} + \frac{1}{r} \frac{\partial}{\partial r} (r \frac{\partial w}{\partial r}) \right) - \frac{\lambda^*}{1 + \lambda} \left( 2u \frac{\partial^3 w}{\partial r^3} + u \frac{\partial^3 u}{\partial z \partial r^2} + w \frac{\partial^3 u}{\partial z^2 \partial r} + 2w \frac{\partial^3 w}{\partial r^2 \partial z} + \frac{\partial^2 u}{\partial z^2} \frac{\partial w}{\partial r} + \frac{\partial^2 u}{\partial r \partial z} \frac{\partial w}{\partial r} + \frac{\partial^2 w}{\partial r^2} \frac{\partial u}{\partial r} + \frac{\partial w}{\partial r} \frac{\partial^2 w}{\partial z \partial r} + \frac{u}{r} \frac{\partial^2 w}{\partial r^2} + \frac{w}{r} \frac{\partial^2 w}{\partial z \partial r} + 3u \frac{\partial^3 u}{\partial z^2 \partial r} + 3w \frac{\partial^3 w}{\partial z^3} + 2 \frac{\partial u}{\partial z} \frac{\partial^2 w}{\partial z \partial r} + 2 \frac{\partial w}{\partial z} \frac{\partial^2 w}{\partial z^2} \right), \tag{4}$$

$$u \frac{\partial T}{\partial r} + w \frac{\partial T}{\partial z} = \alpha_f \frac{\partial^2 T}{\partial z^2} + \tau \left( D_b \left( \frac{\partial T}{\partial z} \frac{\partial C}{\partial z} \right) + \frac{D_t}{T_\infty} \left( \frac{\partial T}{\partial z} \right)^2 \right) + 2\tau \frac{D_t}{T_\infty} \left( u \frac{\partial T}{\partial z} \frac{\partial^2 T}{\partial r \partial z} + w \frac{\partial^2 T}{\partial z^2} \frac{\partial T}{\partial z} \right), \tag{5}$$

$$u \frac{\partial C}{\partial r} + w \frac{\partial C}{\partial z} = \frac{D_t}{T_\infty} \left( u \frac{\partial^3 T}{\partial r \partial z^2} + w \frac{\partial^3 T}{\partial z^3} \right) + D_b \frac{\partial^3 C}{\partial z^3} + \frac{D_t}{T_\infty} \frac{\partial^2 T}{\partial z^2}, \tag{6}$$

The model's physical conditions are defined as:

$$\begin{aligned} u = 0, w = 0, T_w - T = 0, v - r\omega = 0, C - C_w = 0, \text{ at } z = 0, \\ u = 0, w = 0, T - T_\infty = 0, v - r\Omega = 0, C - C_\infty = 0, \text{ at } z = r \tan \gamma. \end{aligned} \tag{7}$$

where  $(u, v, w)$  are components of flow along  $(r, \theta, z)$ , respectively,  $\lambda, \lambda^*$  are the retardation and relaxation times,  $C_p, \nu, \rho$  are heat specific, kinematic viscosity and density,  $k$  and  $\sigma$  are thermal and electrical conductivities. Variables for transformation are described as:

$$\begin{aligned} u = v_f \frac{f(\eta)}{r} = U_w f(\eta), \quad v = v_f \frac{g(\eta)}{r} = U_w g(\eta), \quad w = v_f \frac{h(\eta)}{r} = U_w h(\eta), \\ p = \frac{\rho v_f^2 P}{r^2} = U_w^2 p, \quad \eta = \frac{z}{r}, \quad C - C_\infty = \phi(C_w - C_\infty), \quad T - T_\infty = \Theta(T_w - T_\infty). \end{aligned} \tag{8}$$

The above velocity at the surface is depicted by  $U_w$ . By employing Eq. (8) within Eqs. (1) to (6), we obtain the following relations:

$$\begin{aligned} (1 + \eta^2) f'' + 3f' \eta + (1 + \lambda)(\eta f' f + f^2 - hf' + g^2) - \lambda_1 (2f^3 + \eta^2 f^2 f'' + h^2 f'' - g^2 f + 4\eta f^2 f' - \eta g^2 \\ - 4hff' - 2\eta hff'' - 2fg^2 + 2\eta fgg' - 2hgg' + fg^2) = 0, \end{aligned} \tag{9}$$

$$\begin{aligned} (1 + \eta) g'' + 3f' \eta - (1 + \lambda)(\eta g' f + hg' + 2gf) - \lambda_1 (4\eta f^2 g' + \eta^2 f^2 g'' - 4hgg' - 2\eta hgg'' \\ + g^2 g'' - 2gf^2 + 2\eta gff' - \eta g' g^2) = 0, \end{aligned} \tag{10}$$

$$\begin{aligned} (1 + \eta^2) h'' + (1 + \lambda)(3\eta fh' + h(f + 1 - h') + \eta hf) - \lambda_1 (2hf^2 + \eta^2 hf^2 + \eta^2 h'' f^2 - h'' h^2 \\ - 4hfh' - 2\eta hfh'' - hg^2 - \eta hg^2) = 0, \end{aligned} \tag{11}$$

$$(1 + \eta^2) \Theta'' + \eta \Theta' - \text{Pr}(h - \eta f) \Theta' - (1 + \eta^2) \text{Pr} N_b \Theta' \Phi' + (1 + \eta^2) \text{Pr} N_t (\Theta')^2 = 0, \tag{12}$$

$$(1 + \eta^2) \Phi'' + \eta \Phi' - \text{Sc}(h - \eta f) \Phi' + \frac{N_b}{N_t} ((1 + \eta^2) \Phi'' + \eta \Phi') = 0. \tag{13}$$

The boundary constraints, in their transferred form, can be elucidated as follows:

$$\begin{aligned} f(0) = h(0) = 0, \quad g(0) = \text{Re}_w, \quad \Theta(0) = \Phi(0) = 1, \\ f(\eta_0) = h(\eta_0) = 0, \quad g(\eta_0) = \text{Re}_\Omega, \quad \Theta(\eta_0) = \Phi(\eta_0) = 0. \end{aligned} \tag{14}$$

in which  $\lambda_1 = \lambda^* U_w^2 / \nu_f = \text{Maxwell factor}$ ,  $\lambda = \text{Jeffery fluid parameter}$ ,  $N_t = \tau D_T \nabla T / \nu_f T_\infty = \text{thermophoresis factor}$ ,  $N_b = \tau D_B \nabla C / \nu_f = \text{Brownian motion factor}$ ,  $\text{Pr} = \mu_f (c_p)_f / k_f = \text{Prandtl number}$ ,  $\text{Sc} = \nu_f / D_b = \text{Schmidt number}$ ,  $\text{Re}_w = r^2 \omega / \nu_f = \text{local Reynolds number at disk surface}$  and  $\text{Re}_\Omega = r^2 \Omega / \nu_f = \text{local Reynolds number at cone surface}$ .

### 2.1. Quantities of interest

The primary objects of paramount importance include tangential skin friction =  $C_\theta$ , radial skin friction =  $C_f$ , Nusselt number =  $Nu$ , and Sherwood number =  $Sh$ . The mathematical expressions for these quantities are given as:

$$\begin{aligned} C_{fd} = \frac{\tau_r}{\rho_f U_w^2}, \text{ where } \tau_r = \frac{\mu_f}{1 + \lambda_1} \left[ \frac{\partial u}{\partial z} + \lambda_2 \left( u \frac{\partial^2 u}{\partial r \partial z} + v \frac{\partial^2 u}{\partial z^2} \right) \right]_{z=0, r \tan \gamma} \\ C_{gd} = \frac{\tau_\theta}{\rho_f U_w^2}, \text{ where } \tau_\theta = \frac{\mu_f}{1 + \lambda_1} \left[ \frac{\partial v}{\partial z} + \lambda_1 \left( v \frac{\partial^2 v}{\partial r \partial z} + u \frac{\partial^2 v}{\partial z^2} \right) \right]_{z=0, r \tan \gamma} \end{aligned} \tag{15}$$



$$\begin{aligned}
 Nu &= \frac{rq_w}{k_f(T_w - T_\infty)}, \text{ where } q_w = -k_f \left( \frac{\partial T}{\partial z} \right)_{z=0, r \tan \gamma} = \text{heat transfer rate} \\
 Sh &= \frac{rJ_w}{D_B(T_w - T_\infty)}, \text{ where } J_w = -D_B \left( \frac{\partial C}{\partial z} \right)_{z=0, r \tan \gamma} = \text{mass transfer rate}
 \end{aligned}
 \tag{16}$$

where  $c$  and  $d$  describe cone and disk.

### 3. Framework of Artificial Neural Networks (ANNs)

Recently, ANNs have established a wide range of applications across various industries. ANNs draw inspiration from the structure and functionality of the human brain, gaining popularity for their capacity to effectively replicate intricate and nonlinear functions. One commonly employed ANN model is the multilayer perceptron (MLP) network. The LMLA-BPNN (Levenberg-Marquardt Learning Algorithm with Backpropagation Neural Network) acquires information through the learning process and stores it within inter-neuron networks, represented as "weights" in the layers that connect input, hidden, and output nodes. These weights are organized as two-dimensional arrays of numerical values, reflecting the "strength" of connections between neurons. During computation, these weights are leveraged to calculate the resulting signal values for newly introduced input signals. Each layer within the network is interconnected via numerical units referred to as neurons. The network is subsequently linked to at least one "hidden layer," within which the actual computation occurs through a system of "weighted connections." The "output layer," which is connected to the concealed layers, generates the final output. During the process of backpropagation, there is an error correction mechanism between the predicted and target data. This entails fine-tuning the network's weights and biases by persistently adjusting the input nodes to minimize the error [42]. The training process continues iteratively until the error has been effectively minimized. In this study, various ANN models have been employed to predict the behavior of electromagnetically influenced chemically reactive fluid flow through the gap of the disk cone. Optimizing the dataset used for training plays a crucial role in influencing the prediction accuracy of artificial neural networks (ANNs). In the current problem, ANN model is planned for predicting  $\lambda, M$  against  $g(\eta)$  in four different scenarios like  $Re_\omega = 0, Re_\Omega = 1, Re_\omega = 1, Re_\Omega = 0, Re_\omega = 1, Re_\Omega = 2,$  and  $Re_\omega = -1, Re_\Omega = 1$ . The prediction values obtained are subsequently assessed using a range of metrics, including regression analysis, gradient analysis, accuracy assessment, fitness evaluation, performance analysis, and histogram analysis at the productivity layer. To ensure the ANN model provides precise predictions, it is imperative to optimize the data used during its development [43]. Consequently, the data allocated for training the ANN model has been meticulously divided to achieve the best possible outcomes. Specifically, 10% of the data is reserved for the testing phase, another 10% for the validation phase, and the remaining 80% of the data is utilized for training the ANN model to its fullest potential. The acquired prediction values undergo a comprehensive evaluation employing various metrics, encompassing regression analysis, gradient analysis, accuracy assessment, fitness evaluation, performance analysis, and histogram analysis at the productivity layer. Ensuring the ANN model delivers accurate predictions necessitates meticulous data optimization during its development [43]. As a result, the dataset designated for training the ANN model has been thoughtfully partitioned to optimize results: 10% is set aside for the testing phase, another 10% for validation, and the remaining 80% is dedicated to training the ANN model to its maximum capability. There is no generally recognized approach for determining the optimal number of neurons to use in ANNs [44]. In order to tackle the fluidic problem using a sigmoid activation function, the neural networks (NNs) proposed in this study are configured with a parallel architecture consisting of ten high-processing neurons. The input values for the sigmoid activation function fall within the range of +1 to 0, as depicted in Fig 2. This function displays a smooth, S-shaped, and nonlinear behavior.

The Levenberg-Marquardt training algorithm, known as LMTA, is a powerful and widely adopted training method in the literature, often favored by researchers when designing ANN models [45]. In this ANN model, the Tan-Sig function is employed for the hidden nodes, while the Purelin function is used for the output nodes [46]. The transfer functions are configured as follows:

$$\tilde{f}(x) = \frac{1}{1 + e^{-x}}
 \tag{17}$$

Following the development of ANN models, the critical next step is to analyze their prediction performance. The following formulas are applied to compute the R and MSE values [47]:

$$MSE = \frac{1}{n} \sum_{i=1}^n (X_{e^i} - X_{ANN(i)})^2,
 \tag{18}$$

$$R = \sqrt{1 - \frac{\sum_{i=1}^n (X_{e^i} - X_{ANN(i)})^2}{\sum_{i=1}^n (X_{e^i})^2}},
 \tag{19}$$

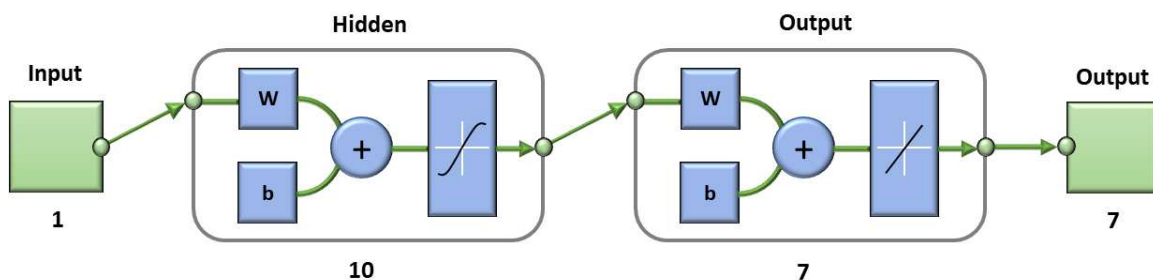


Fig. 2. Neural Network Diagram for LMS-NNA.



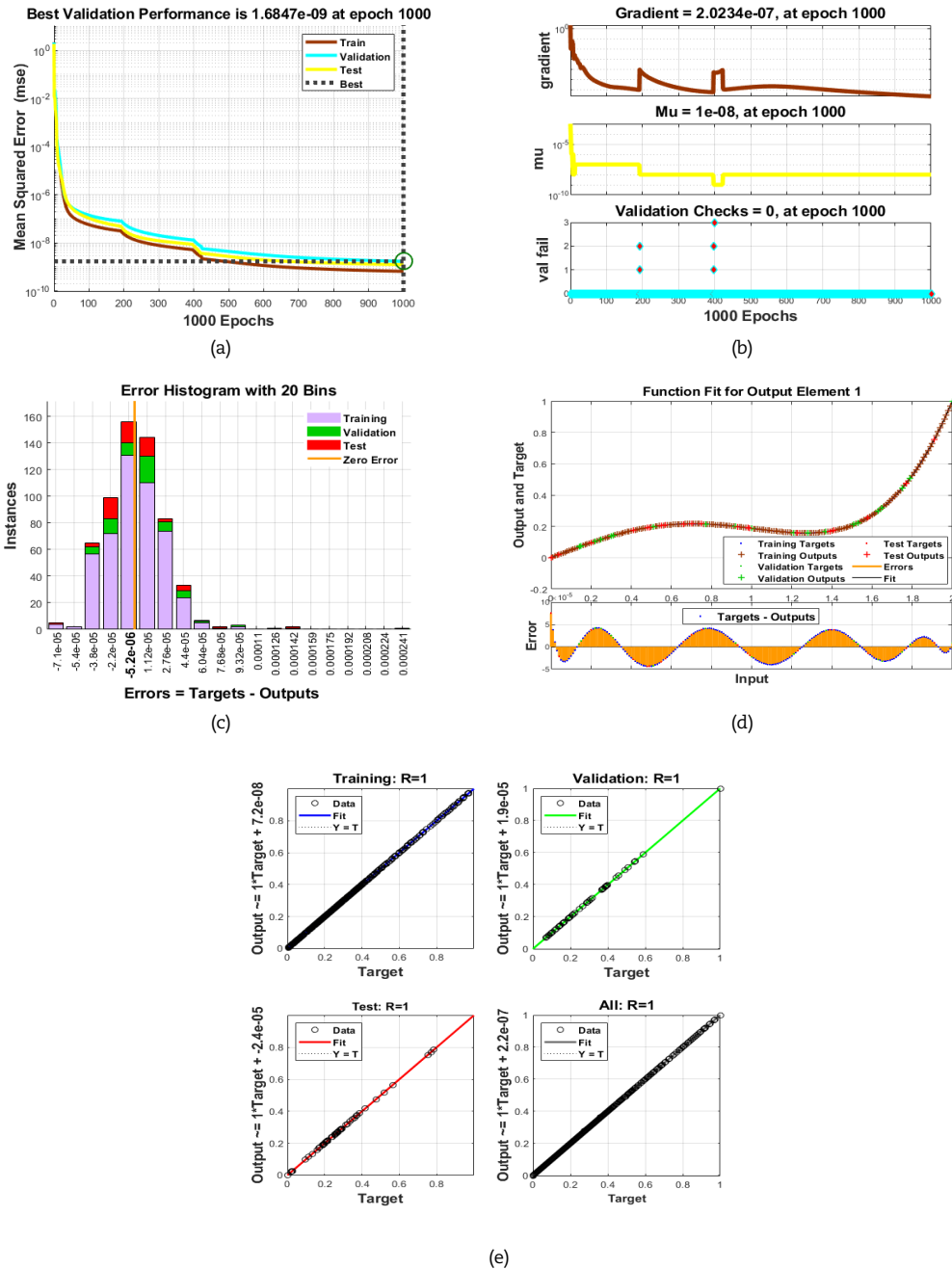


Fig. 3. Plots LMS-NNA design for  $g(\eta)$  on transverse velocity  $g(\eta)$  of the HIE-PNF-NFDDT fluid model when  $Re_\omega = 0, Re_\eta = 1$   
 (a) MSE outcomes (b) Transition state (c) Error histogram (d) Curve fitting (e) Regression.

Another essential metric employed to assess the effectiveness of ANN models is the error between the predicted and target data, for which the following relationship is utilized:

$$\% \text{Error rate} = \left( \frac{X_{\text{exp}} - X_{\text{ANN}(i)}}{X_{\text{exp}}} \right) \times 100 \tag{20}$$

#### 4. Interpretation of Numerical Results

The ANN models are represented visually in Figs. 3(a-e) during the training phase. These figures are crafted to illustrate the LMS-NNA, which explains the transverse velocity  $g(\eta)$  against the Jeffery fluid parameter  $\lambda$  of fluid model in terms of MSE outcomes, error histograms, transition states, regression analysis, and fitting curves. It is evident from this figure that the depiction provides excellent validation. Figure 3(a) is specifically designed to showcase the Mean Square Error (MSE) for scenario  $Re_\omega = 0, Re_\eta = 1$ , with static disk and gyrating cone by keeping 1000 epochs with excellent authentication depiction is  $1.6847 \times 10^{-9}$ . The gradient serves as a vector guiding the network with precise magnitude and direction, aimed at achieving the desired evaluation as swiftly as possible. Conversely, "mu" is a parameter that facilitates a specific procedure, and its value accurately reflects the solution's convergence.



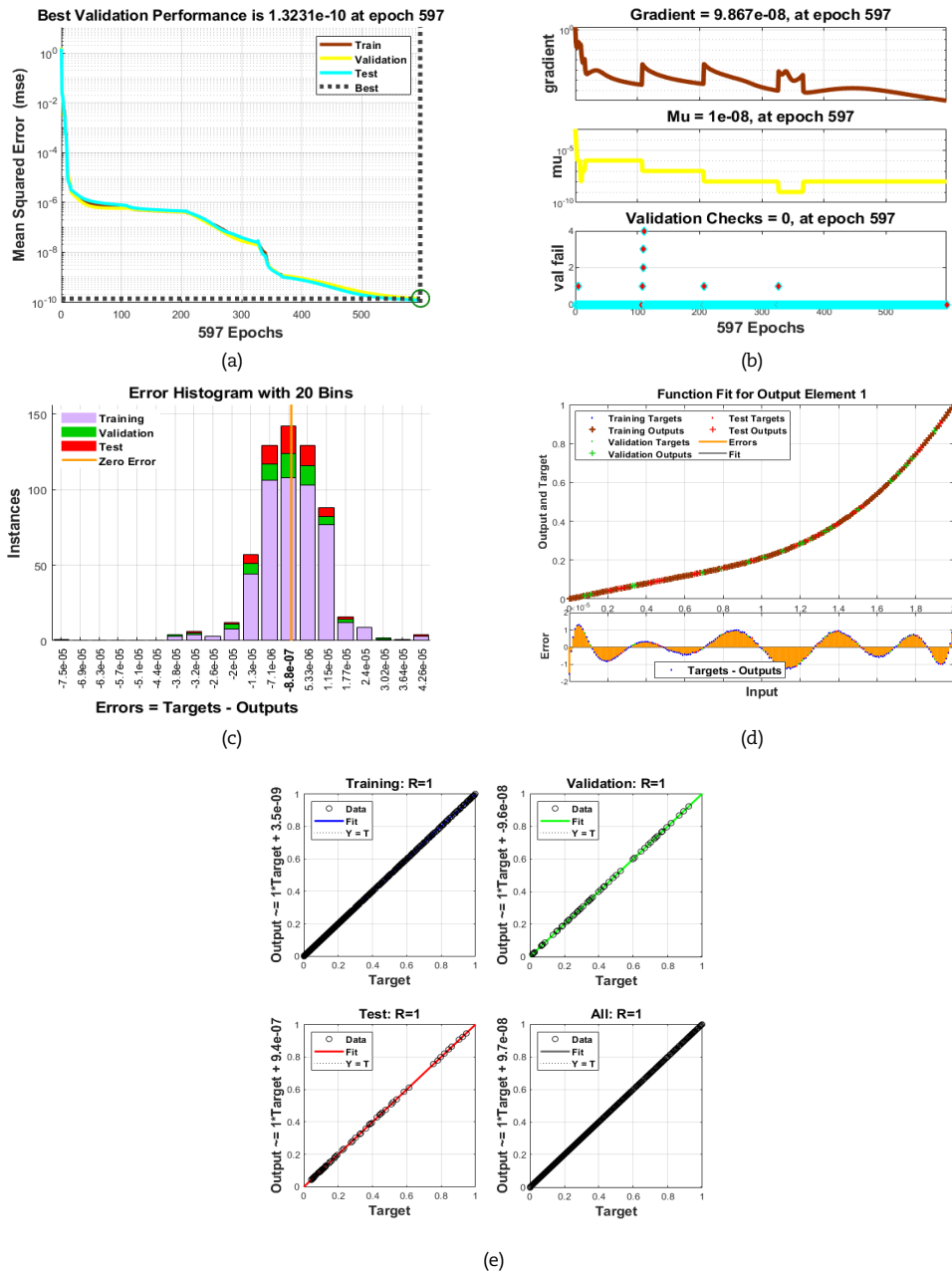


Fig. 4. Plots LMS-NNA for the impact of  $M$  on transverse velocity  $g(\eta)$  of the HIE-PNF-NFDDT fluid model when  $Re_w = 0, Re_\Omega = 1$   
 (a) MSE outcomes (b) Transition state (c) Error histogram (d) Curve fitting (e) Regression.

Figure 3(b) provides a detailed explanation of "mu," gradient, and validation within the context of  $Re_w = 0, Re_\Omega = 1$ . Error histograms offer an additional avenue for assessing the nearness of estimated values to reference values. This graphical view depicts the dissemination of errors, illustrating the deviations of all evaluated values from the zero-error point. Figure 3(c) illustrates the error histogram, enabling a comparison of the first scenario's performance with 20 bins. The fitness evaluation graphs for the network models depict the errors resulting from disparities between the reference and target solutions. Detailed curve fitting information for the current problem is presented in Fig. 3(d). Regression is a graphical technique employed to assess the accuracy of estimated values concerning reference values for testing points, validation, and training. The numerical value of the regression serves as a measure to evaluate the precision and accuracy of the numerical outcomes. An R value of 1 signifies a close match between the estimated values and the reference values, while an R value of 0 indicates a weak association between the estimated and reference values. Figure 3(e) illustrates the regression analysis for the scenario  $Re_w = 0, Re_\Omega = 1$ , pertaining to fluid flow through static disk and gyrating cone. The training performances of the ANN model are depicted in Figs. 4(a-e) for variation in magnetic factor  $M$  against  $g(\eta)$ . It is evident from these figures that the optimal validation performance is achieved and is  $1.3231 \times 10^{-10}$  at epoch 597. These figures are specifically created to illustrate the LMS-NNA, which elucidates the transverse velocity of fluid model, comprising MSE findings, error histograms, transition states, regression analyses, and fitting curves for the scenario  $Re_w = 0, Re_\Omega = 1$ , pertaining to fluid flow through gyrating cone and static disk gap. Figures 5(a-e) have been crafted to illustrate the LMS-NNA which explains the transverse velocity  $g(\eta)$  against Jeffrey fluid parameter  $g(\eta)$  for the scenario  $Re_w = 1, Re_\Omega = 0$ . These figures are explaining  $g(\eta)$  for HIE-PNF-NFDDT fluid model pertaining to fluid flow and encompassing MSE results, transition states, error histograms, fitting curves, and regression analysis. It is evident from these figures that the optimal validation performance  $2.1258 \times 10^{-9}$  has been achieved at epoch 597.



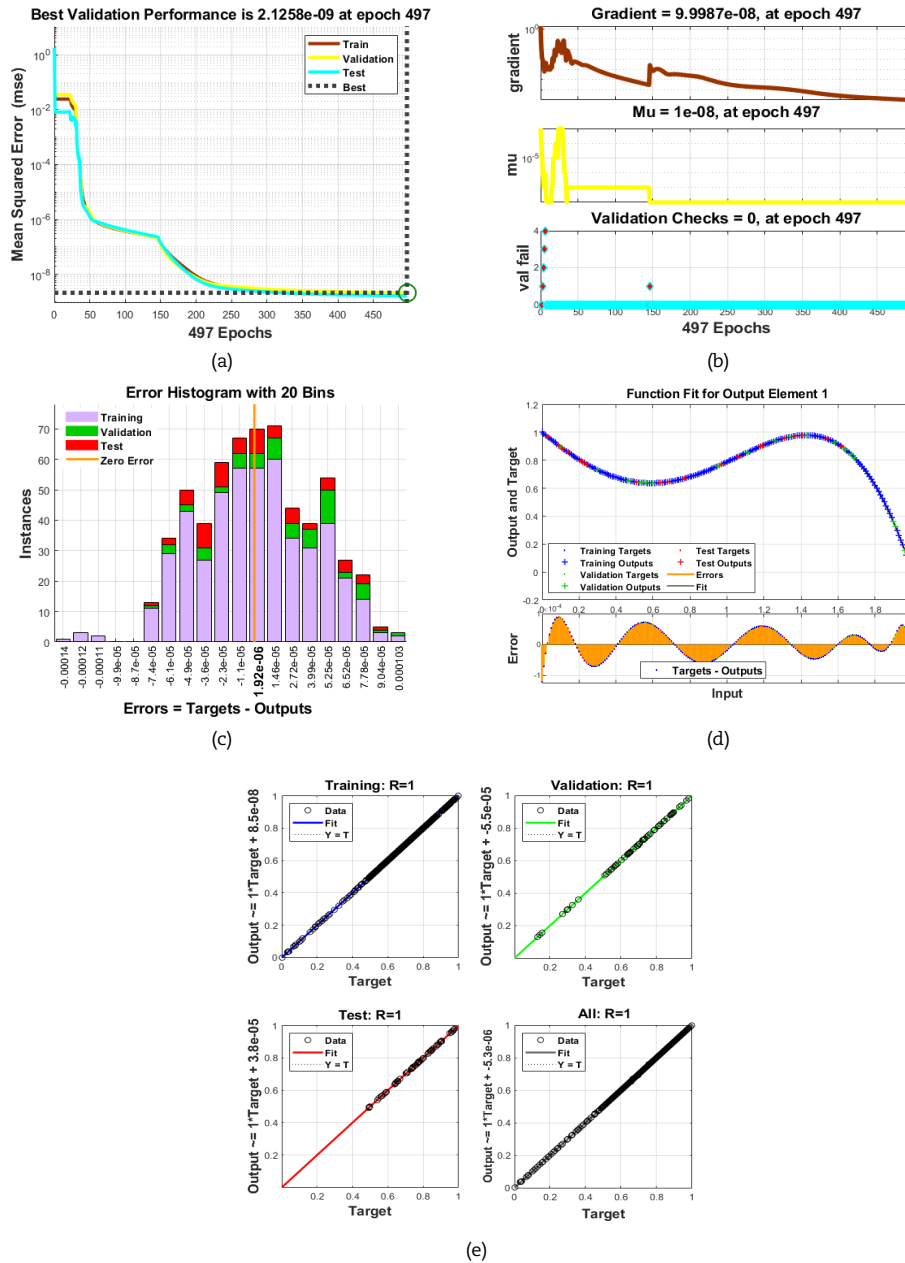


Fig. 5. Plots LMS-NNA design for the impact of  $g(\eta)$  on transverse velocity  $g(\eta)$  of the HIE-PNF-NFDDT fluid model  $Re_w = 1, Re_\Omega = 0$  (a) MSE outcomes (b) Transition state (c) Error histogram (d) Curve fitting (e) Regression.

Figures 6(a-e) have been crafted to illustrate the LMS-NNA which explains the transverse velocity  $g(\eta)$  against magnetic factor  $M$  for the scenario  $Re_w = 1, Re_\Omega = 0$ . These figures are explaining  $g(\eta)$ , for fluid model pertaining to fluid flow and encompassing MSE results, transition states, error histograms, fitting curves, and regression analysis. It is evident from these figures that the optimal validation performance  $6.7661 \times 10^{-11}$  has been achieved at epoch 909. Figures 7(a-e) have been crafted to illustrate the LMS-NNA which explains the transverse velocity  $g(\eta)$  against Jeffery fluid factor  $\lambda$  for the scenario  $Re_w = 1, Re_\Omega = 2$ . These figures are explaining  $g(\eta)$  for fluid model pertaining to fluid flow through the space between cone and gap, with cone and disk gyrating in same directions and encompassing MSE results, transition states, error histograms, fitting curves, and regression analysis. It is evident from these figures that the optimal validation performance  $6.2883 \times 10^{-10}$  has been achieved at epoch 1000. Figures 8(a-e) have been crafted to illustrate the LMS-NNA which explains the transverse velocity  $g(\eta)$  against the magnetic factor  $M$  for the scenario  $Re_w = 1, Re_\Omega = 2$ . These figures explain  $g(\eta)$  for fluid model pertaining to fluid flow and encompassing MSE results, transition states, error histograms, fitting curves, and regression analysis. It is evident from these figures that the optimal validation performance  $2.2169 \times 10^{-10}$  has been achieved at epoch 1000. Figures 9(a-e) have been crafted to illustrate the LMS-NNA which explains the transverse velocity  $g(\eta)$  against Jeffery fluid factor  $\lambda$  for the scenario  $Re_w = -1, Re_\Omega = 1$ . These figures are explaining  $g(\eta)$  for fluid model pertaining to fluid flow and encompassing MSE results, transition states, error histograms, fitting curves, and regression analysis. It is evident from these figures that the optimal validation performance  $1.8409 \times 10^{-8}$  has been achieved at epoch 1000. Figures 10(a-e) have been crafted to illustrate the LMS-NNA which explains the transverse velocity  $g(\eta)$  against magnetic factor  $M$  for the scenario  $Re_w = -1, Re_\Omega = 1$ . These figures are explaining the transverse velocity of the HIE-PNF-NFDDT fluid model pertaining to fluid flow through the space between cone and gap, with cone and disk gyrating in opposite directions and encompassing MSE results, transition states, error histograms, fitting curves, and regression analysis. It is evident from these figures that the optimal validation performance  $2.8227 \times 10^{-9}$  has been achieved at epoch 1000.





Table 1. Consequences of LMS-NNA for different scenarios of NCM-HMTMNF-NNA.

Cases	MSE			Performance	Gradient	Mu	Epoch	Time (s)
	Training	Validation	Testing					
1	$2.4828 \times 10^{-10}$	$2.6846 \times 10^{-9}$	$1.2203 \times 10^{-9}$	$6.48 \times 10^{-10}$	$2.02 \times 10^{-7}$	$1.00 \times 10^{-8}$	1000	03
2	$1.2435 \times 10^{-10}$	$1.3231 \times 10^{-10}$	$1.1530 \times 10^{-10}$	$1.24 \times 10^{-10}$	$9.87 \times 10^{-8}$	$1.00 \times 10^{-8}$	597	02
3	$1.7365 \times 10^{-9}$	$2.1257 \times 10^{-9}$	$1.6269 \times 10^{-10}$	$1.74 \times 10^{-9}$	$1.00 \times 10^{-7}$	$1.00 \times 10^{-8}$	497	01
4	$5.7223 \times 10^{-11}$	$6.7660 \times 10^{-11}$	$5.2680 \times 10^{-11}$	$5.72 \times 10^{-11}$	$9.97 \times 10^{-8}$	$1.00 \times 10^{-9}$	909	03
5	$6.6741 \times 10^{-10}$	$6.2883 \times 10^{-10}$	$1.0043 \times 10^{-9}$	$6.67 \times 10^{-10}$	$2.70 \times 10^{-6}$	$1.00 \times 10^{-9}$	1000	04
6	$2.7329 \times 10^{-10}$	$2.2168 \times 10^{-10}$	$2.4718 \times 10^{-10}$	$2.73 \times 10^{-10}$	$6.13 \times 10^{-7}$	$1.00 \times 10^{-8}$	1000	04
7	$1.4310 \times 10^{-8}$	$1.8409 \times 10^{-8}$	$1.5822 \times 10^{-8}$	$1.43 \times 10^{-8}$	$5.66 \times 10^{-7}$	$1.00 \times 10^{-7}$	1000	04
8	$4.4185 \times 10^{-9}$	$2.8229 \times 10^{-9}$	$6.4444 \times 10^{-9}$	$4.42 \times 10^{-9}$	$2.20 \times 10^{-6}$	$1.00 \times 10^{-8}$	1000	04

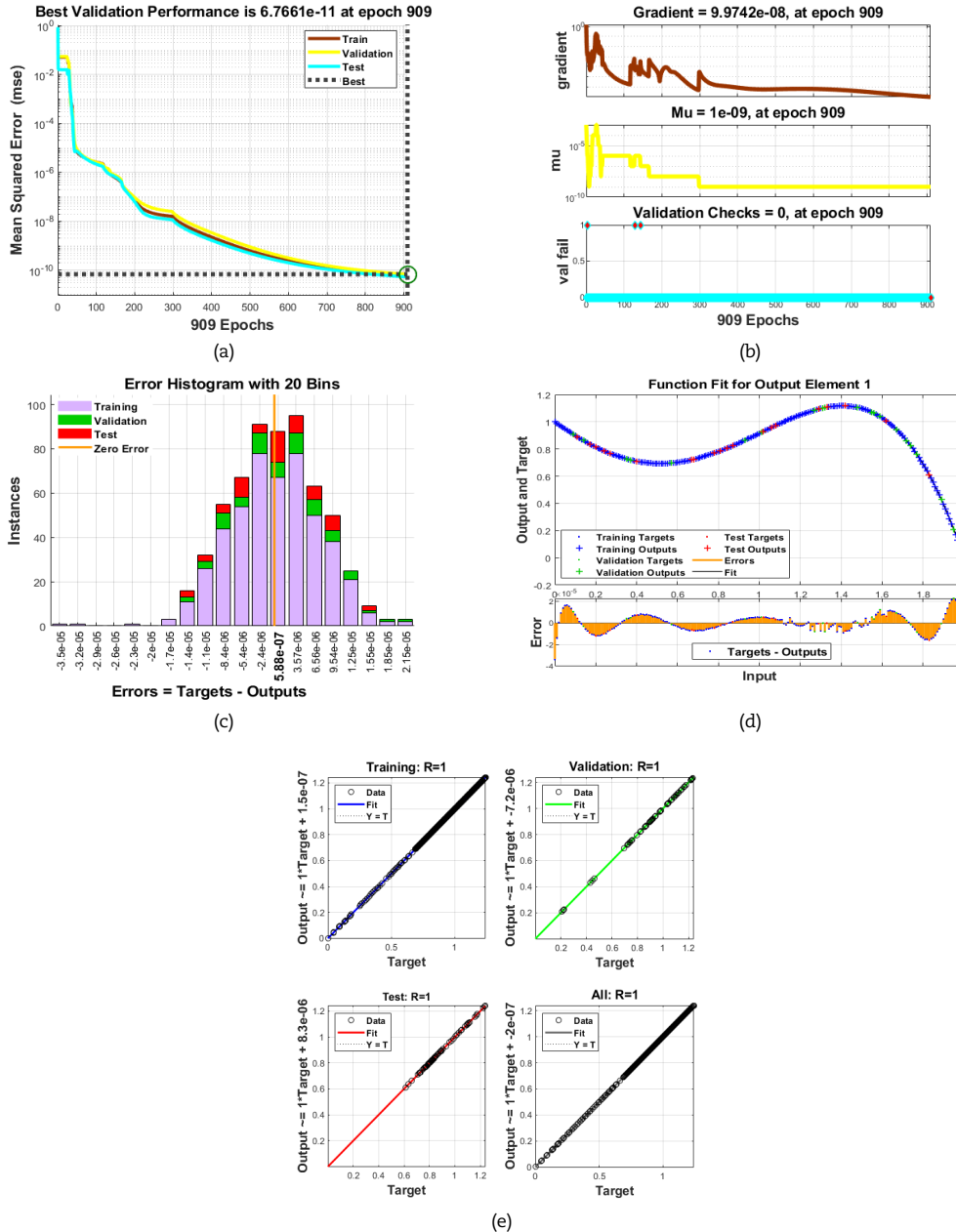


Fig. 6. Plots LMS-NNA design for the impact of M on transverse velocity  $g(\eta)$  of the HIE-PNF-NFDDT fluid model  $Re_w = 1, Re_\Omega = 0$  (a) MSE outcomes (b) Transition state (c) Error histogram (d) Curve fitting (e) Regression.

Table 1 presents a collection of computational values for various factors in the ANN models. The table includes distinct computational values for MSE, performance, gradient, and mu, across different epochs (1000, 597, 497, 909, 1000, 1000, 1000, 1000) for all the four scenarios comprising of (i) static cone and gyrating disk  $Re_w = 0, Re_\Omega = 1$ , (ii) static disk and gyrating cone  $Re_w = 1, Re_\Omega = 0$ , (iii) cone and disk move in similar direction  $Re_w = 1, Re_\Omega = 2$ , (iv) cone and disk move in reverse directions  $Re_w = -1, Re_\Omega = 1$ . The table is constructed for impacts of variations in Jeffrey fluid factor  $\lambda$  and magnetic factor M against transverse velocity distribution  $g(\eta)$ .



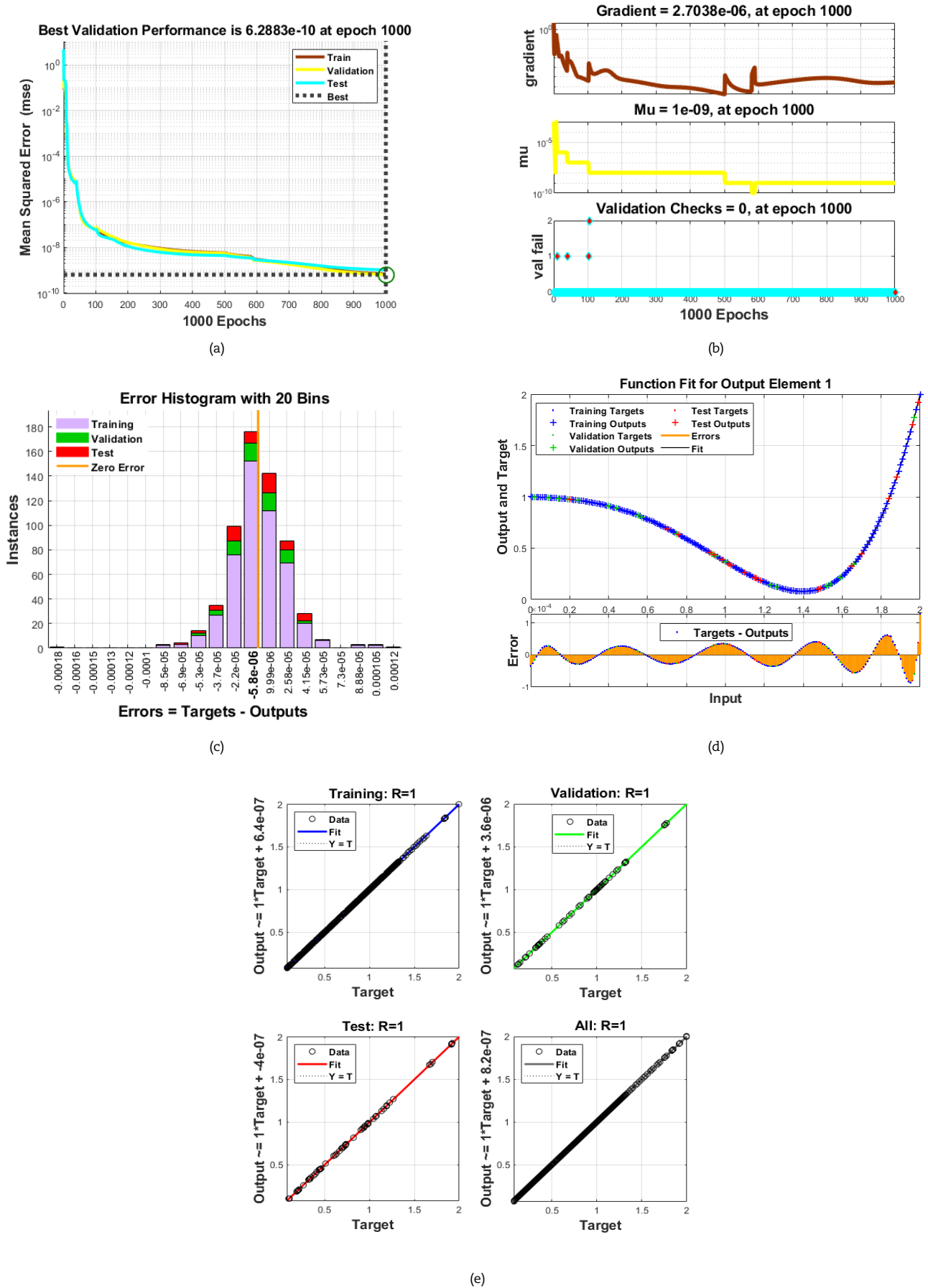


Fig. 7. Plots LMS-NNA design for the impact of  $g(\eta)$  on transverse velocity  $g(\eta)$  of the HIE-PNF-NFDDT fluid model  $Re_w = 1$ ,  $Re_u = 2$   
 (a) MSE outcomes (b) Transition state (c) Error histogram (d) Curve fitting (e) Regression.



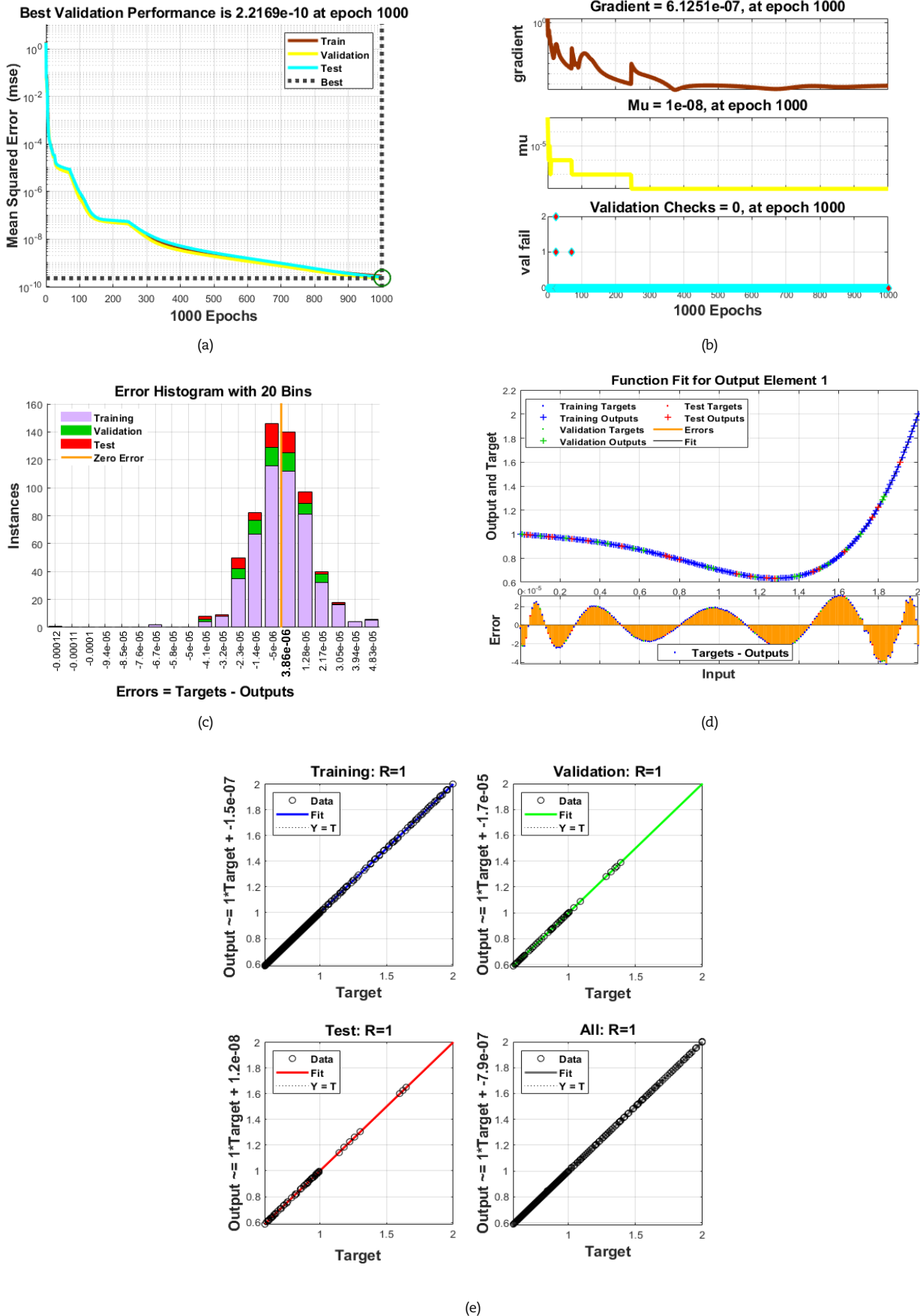
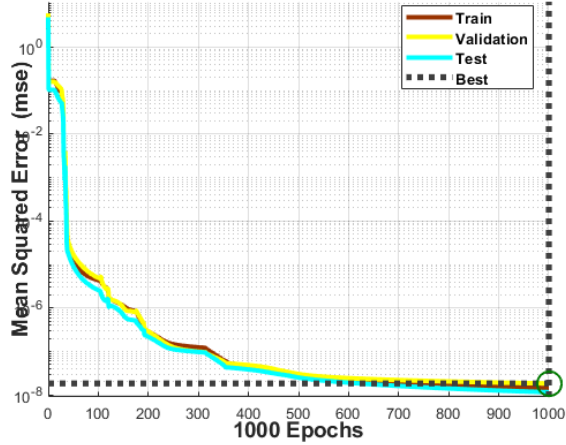


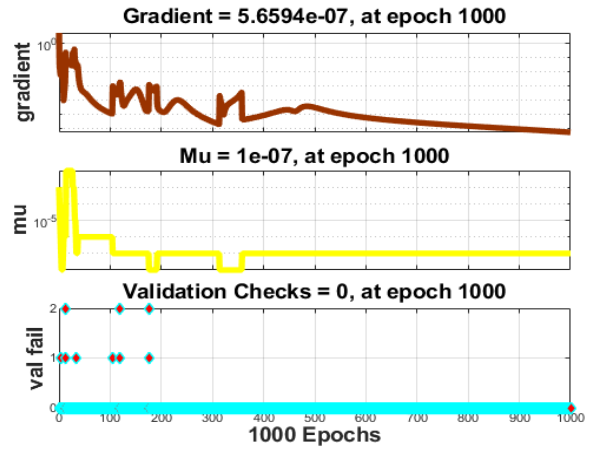
Fig. 8. Plots LMS-NNA design for impact of  $M$  on transverse velocity  $g(\eta)$  of the HIE-PNF-NFDDT fluid model  $Re_w = 1, Re_{\eta} = 2$   
 (a) MSE outcomes (b) Transition state (c) Error histogram (d) Curve fitting (e) Regression.



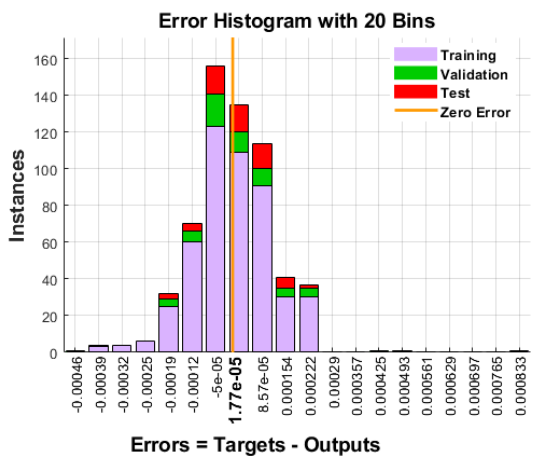
Best Validation Performance is 1.8409e-08 at epoch 1000



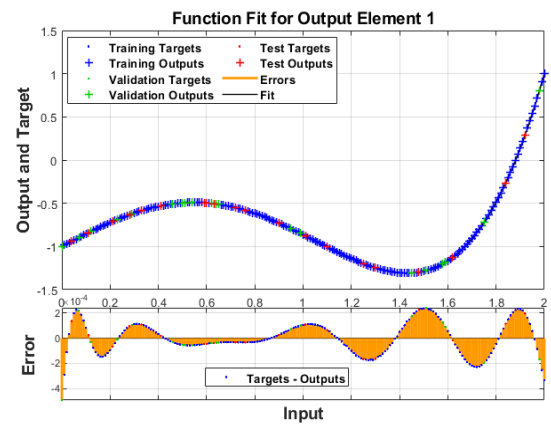
(a)



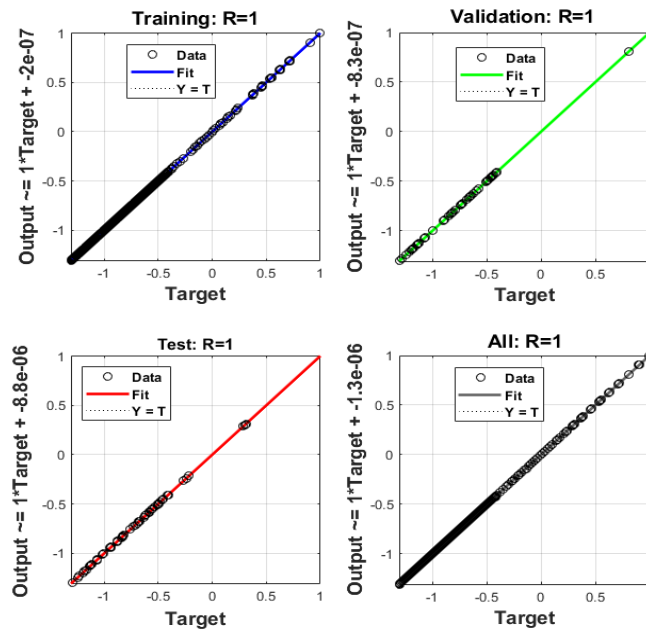
(b)



(c)



(d)



(e)

Fig. 9. Plots LMS-NNA design for the impact of  $g(\eta)$  on transverse velocity  $g(\eta)$  of the HIE-PNF-NFDDT fluid model  $Re_w = -1$ ,  $Re_n = 1$  (a) MSE outcomes (b) Transition state (c) Error histogram (d) Curve fitting (e) Regression.



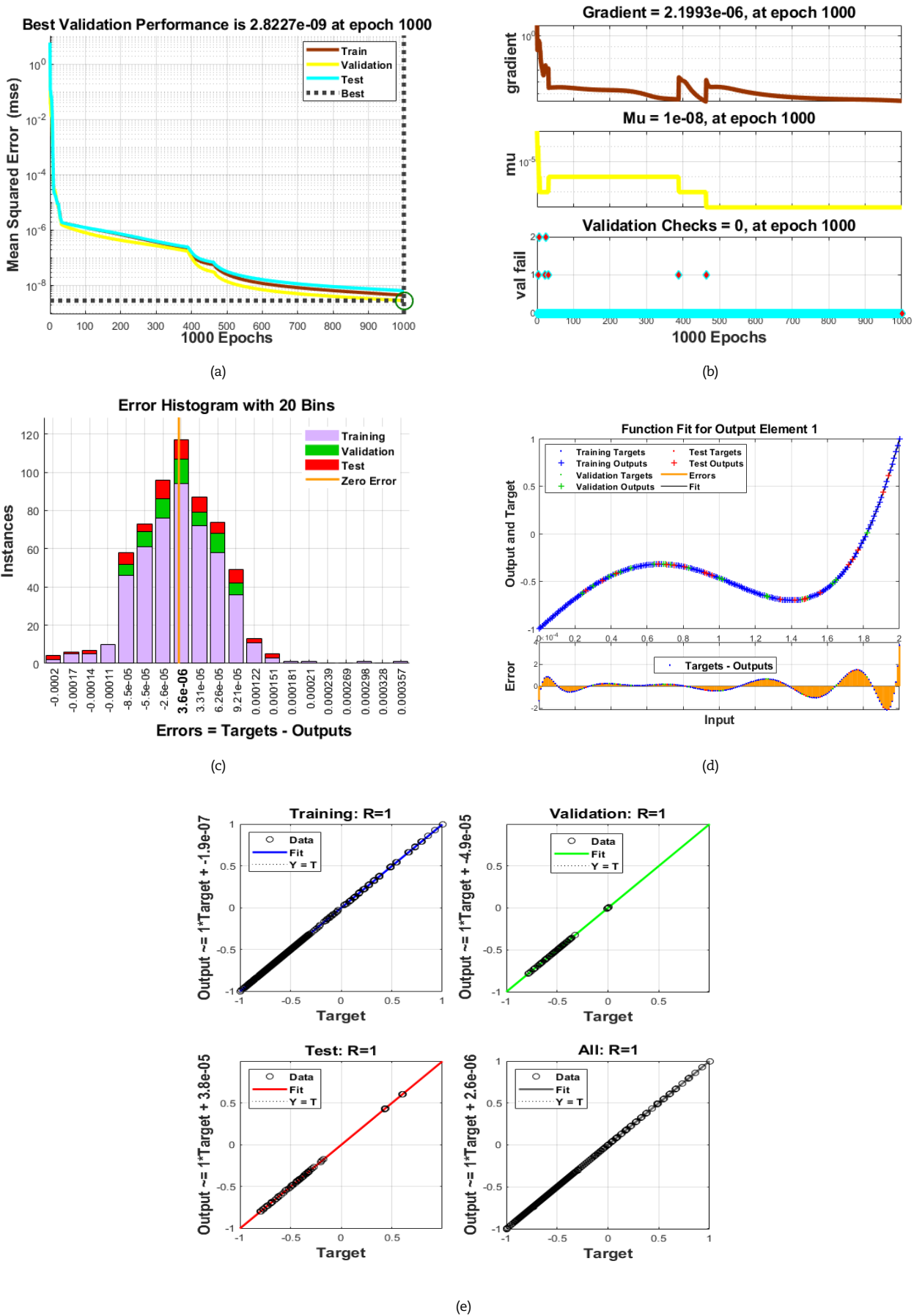


Fig. 10. Plots LMS-NNA design for the impact of  $M$  on transverse velocity  $g(\eta)$  of the HIE-PNF-NFDDT fluid model  $Re_w = -1$ ,  $Re_{ii} = 1$   
 (a) MSE outcomes (b) Transition state (c) Error histogram (d) Curve fitting (e) Regression.



Figures 11 to 18 have been sketched to illustrate the impacts of different emerging factors on transverse velocity distribution. These variations in  $g(\eta)$  have been evaluated against different values of magnetic factor  $M$  and Jeffery fluid factor  $\lambda$  in different scenarios namely; (i) static cone and gyrating disk  $Re_\omega = 0, Re_\Omega = 1$ , (ii) static disk and gyrating cone  $Re_\omega = 1, Re_\Omega = 0$ , (iii) cone and disk move in similar direction  $Re_\omega = 1, Re_\Omega = 2$ , (iv) cone and disk move in reverse directions  $Re_\omega = -1, Re_\Omega = 0$ . In the first scenario the cone is static and disk is spinning i.e.  $Re_\omega = 0, Re_\Omega = 1$  as portrayed in Figs. 11 and 12, with influences of  $\lambda$  and  $M$  against  $g(\eta)$ . From Fig. 11, it is quite obvious that  $g(\eta)$  weakens with greater values of  $\lambda$ . Clearly  $\lambda$  characterizes the rheological behavior of the fluid. In case of transverse velocity distribution, the factor  $\lambda$  reveals the fluid's confrontation to deformation when subjected to shear forces. A higher  $\lambda$  indicates a higher resistance to shear deformation. Therefore, when the  $\lambda$  upsurges, it means that the fluid becomes more resistant to shearing. This resistance results reduction in  $g(\eta)$ . In other words, the fluid is less prone to flow in the transverse direction under the same external conditions. It becomes more viscous in response to shear forces, and this stiffness limits the lateral movement of fluid particles. Hence, with the upsurge in  $\lambda$  a reduction in  $g(\eta)$  has been noticed. Figure 12 examines the impact of  $M$  against  $g(\eta)$ . An increase in  $M$  signifies the strengthening of magnetic forces within the fluid. These magnetic forces induce Lorentz forces that act perpendicular to both the magnetic field and the fluid velocity, effectively restraining the transverse movement of fluid particles. As  $M$  grows, these restraining forces become more prominent, inhibiting the natural tendency of fluid particles to disperse or move transversely. This leads to a decline in  $g(\eta)$ , as the fluid particles are compelled to align more closely along the magnetic field lines and move predominantly in the axial direction of the gap. Actually, the observed retardation in the transverse velocity of fluid flow through the disc and cone gap, stemming from the increasing magnetic factor and Jeffery fluid factor, unfolds a complex interaction between fluid rheology, magnetic forces, and fluid dynamics. The augmentation of the magnetic factor suggests a strengthening influence of magnetic fields on the fluid, imposing additional resistance to its motion. This magnetic factor-induced retardation is particularly evident when coupled with the growing Jeffery fluid factor, representing the elasticity of the fluid. Higher Jeffery fluid factors imply increased resistance to deformation, akin to elastic materials resisting flow. In the engineering context, these phenomena bear significance for a spectrum of applications as discussed below. In scenarios involving a static cone and gyrating disc, or a static disc and gyrating cone, the fluid experiences compounded effects. The static cone or disc serves as a reference point, resisting the rotational forces applied by the gyrating counterpart. The combination of magnetic forces and increased fluid elasticity intensifies the hindrance to transverse flow, leading to a more pronounced retardation. This observation is pivotal in the design of mixing systems, especially in chemical manufacturing processes. In scenarios where the cone and disk are gyrating in the same direction, the fluid encounters a dynamic interaction between their rotational movements. The magnetic and Jeffery fluid factors, when both on the rise, contribute to a collective effect that impedes the transverse flow. This phenomenon finds relevance in the field of mechanical engineering, particularly in the design of rotating machinery such as pumps and turbines. Conversely, when the cone and disk are gyrating in opposite directions, the opposing rotational forces lead to a distinctive dynamic scenario. Here, the combined effect of increasing magnetic and Jeffery fluid factors introduces unique challenges. This configuration finds application in fluidic devices used in biomedical engineering, where precise control of fluid flow is essential. The retardation in transverse velocity, influenced by both magnetic and rheological factors, can impact the accuracy and efficiency of fluidic systems employed in tasks such as drug delivery or diagnostic assays. Engineers need to account for these factors to design fluidic devices that reliably and accurately manipulate fluids for biomedical applications. So, in the remaining three scenarios i.e. static disk and gyrating cone ( $Re_\omega = 1, Re_\Omega = 0$ ), cone and disk gyrating in the same direction i.e. ( $Re_\omega = 1, Re_\Omega = 2$ ), cone and disk gyrating in opposite directions ( $Re_\omega = -1, Re_\Omega = 1$ ), we have observed that the transverse velocity distribution  $g(\eta)$  is a retarding function of both  $\lambda$  and  $M$  as depicted in Figures 13(a), 14(a), 15(a), 16(a), 17(a) and 18(a). The analysis of absolute error (AE) for the developed ANN (artificial neural network) models is illustrated in Figures 11(b), 12(b), 13(b), 14(b), 15(b), 16(b), 17(b) and 18(b) to verify their adherence to correctness criteria. The computed absolute error values for each model are situated within the distinct predefined ranges  $10^{-7}$  to  $10^{-3}$  and  $10^{-8}$  to  $10^{-4}$  for their respective ANN configurations. These numerical absolute error findings, when compared with reference outputs, confirm a commendable level of accuracy, thereby affirming the validity and reliability of the designed ANN models. The comparison of the proposed model is compared with [4, 5] including common parameters as shown in Table 2. The closed agreement verified the obtained results.

**4.1. Potential applications of the current flow problem**

Fluid flow through the disc-cone gap has numerous applications in various fields due to its unique characteristics and versatile nature. The disc-cone configuration refers to a system where a disc-shaped object is positioned in close proximity to a cone-shaped object, creating a gap through which fluid can flow. This design is utilized in different applications to achieve specific objectives. Here are some notable applications:

**(a) Chemical Processing Systems:**

Scenario (i) Static Cone and Gyrating Disk: In chemical reactors, where mixing is crucial for achieving uniform reactions, the retardation in transverse velocity can impact the efficiency of mixing and the overall reaction kinetics. Permissive effects of magnetic and rheological factors are vital in optimizing the design of chemical processing systems.

**(b) Rotating Machinery Design:**

Scenario (ii) Static Disk and Gyrating Cone: The retardation in fluid flow is relevant in the design of rotating machinery such as pumps and turbines. Engineers need to consider the magnetic and rheological influences when designing these systems to ensure efficient energy conversion and transmission.

**Table 2.** Validation of the results of present work with existing literature for  $Pr = 11$ .

Models	Ref. [4]		Ref. [5]		Present work	
$Re_\omega =$ Disk rotation, $Re_\Omega =$ Cone rotation	$\theta'(0)$	$\theta'(\eta_0)$	$\theta'(0)$	$\theta'(\eta_0)$	$\theta'(0)$	$\theta'(\eta_0)$
$Re_\omega = 1, Re_\Omega = 1$	10.276186	6.76871988	10.268926	6.78923871	10.26765922	6.782871023
$Re_\omega = 1, Re_\Omega = 0$	12.326751	10.3287911	12.3108712	10.378879	12.31216871	10.37721901
$Re_\omega = -1, Re_\Omega = 1$	13.341562	9.78290221	13.3389201	9.7652129	13.3356219	9.764271895
$Re_\omega = 0, Re_\Omega = 1$	11.767189	9.8921082	11.75983009	9.87821212	11.75327818	9.876372882



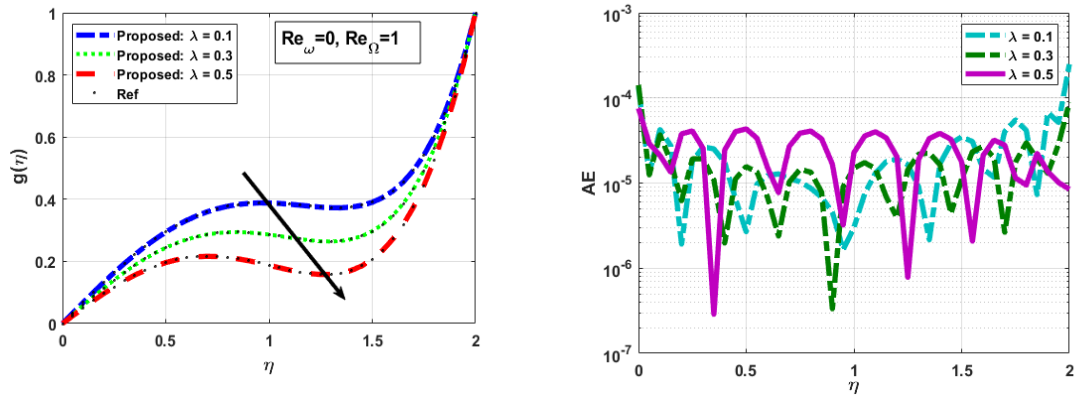


Fig. 11. (a) Variation in  $\lambda$  vs  $g(\eta)$  (b) AE for  $\lambda$ .

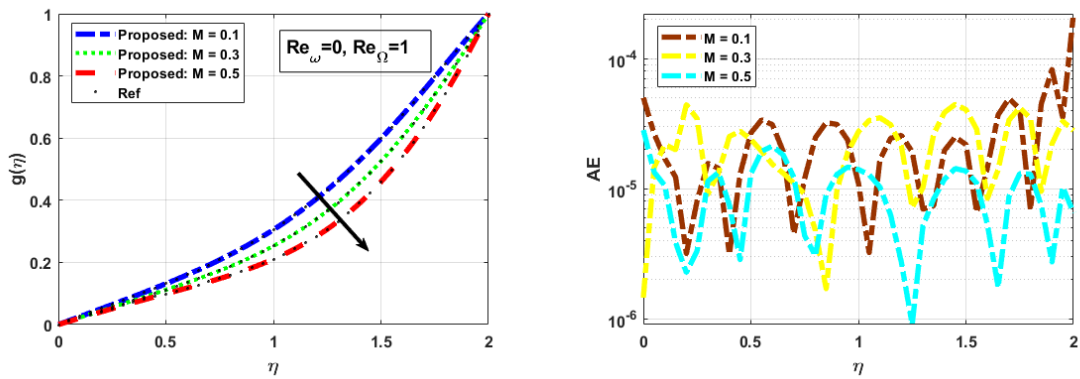


Fig. 12. (a) Variation in  $M$  vs  $g(\eta)$  (b) AE for  $M$ .

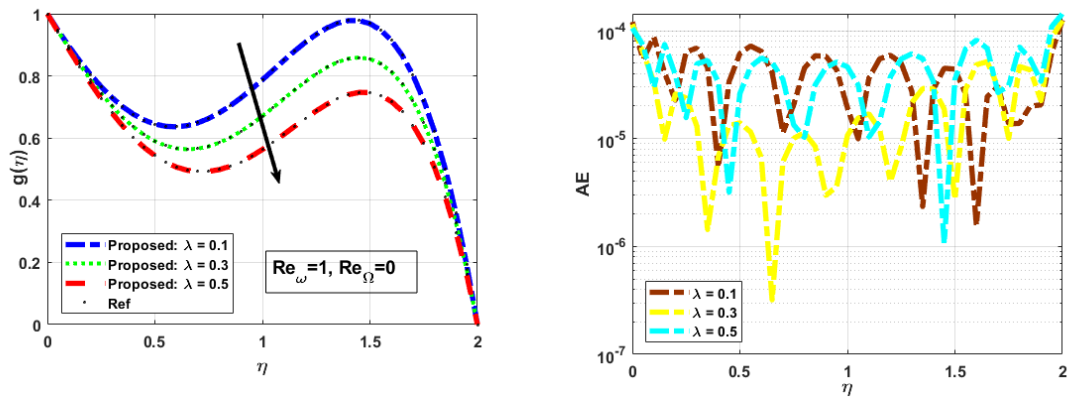


Fig. 13. (a) Variation in  $\lambda$  vs  $g(\eta)$  (b) AE for  $\lambda$ .

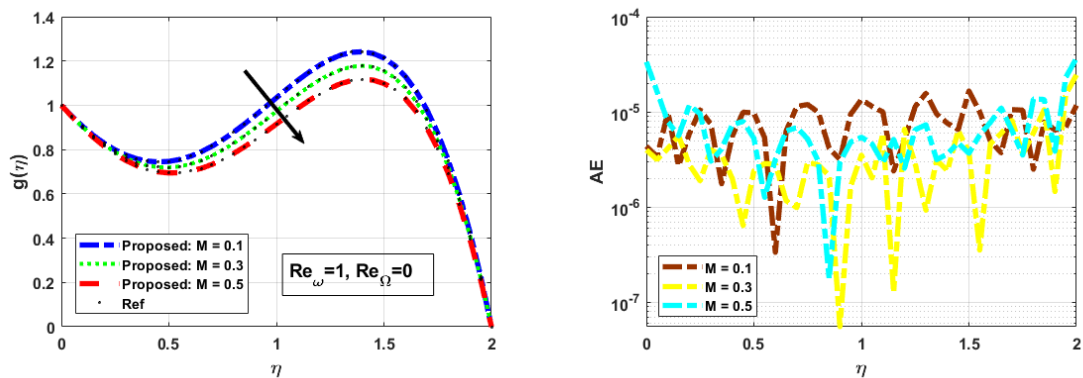


Fig. 14. (a) Variation in  $M$  vs  $g(\eta)$  (b) AE for  $M$ .



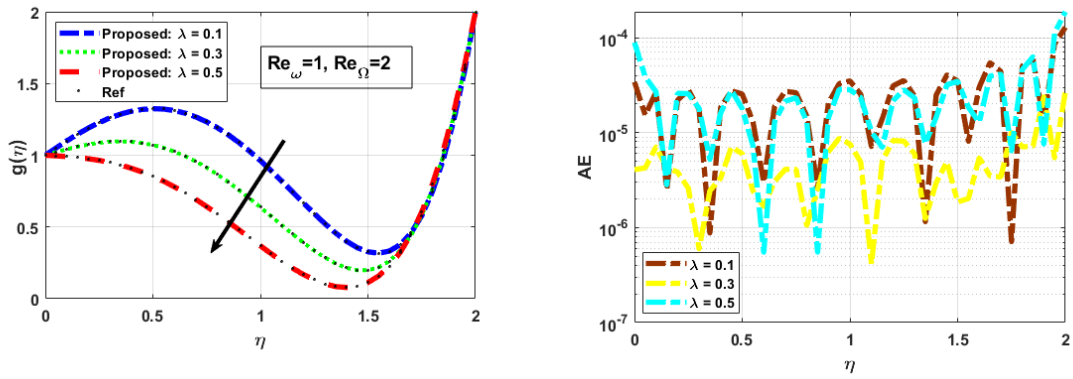


Fig. 15. (a) Variation in  $\lambda$  vs  $g(\eta)$  (b) AE for  $\lambda$ .

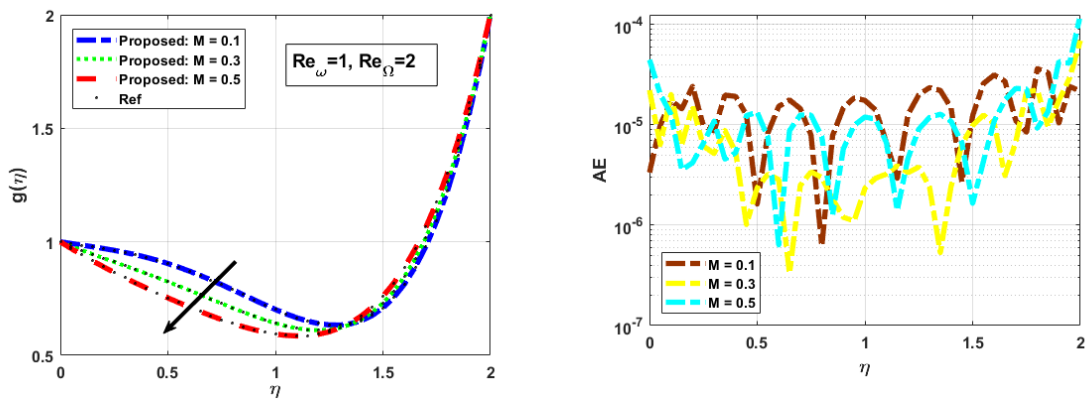


Fig. 16. (a) Variation in  $M$  vs  $g(\eta)$  (b) AE for  $M$ .

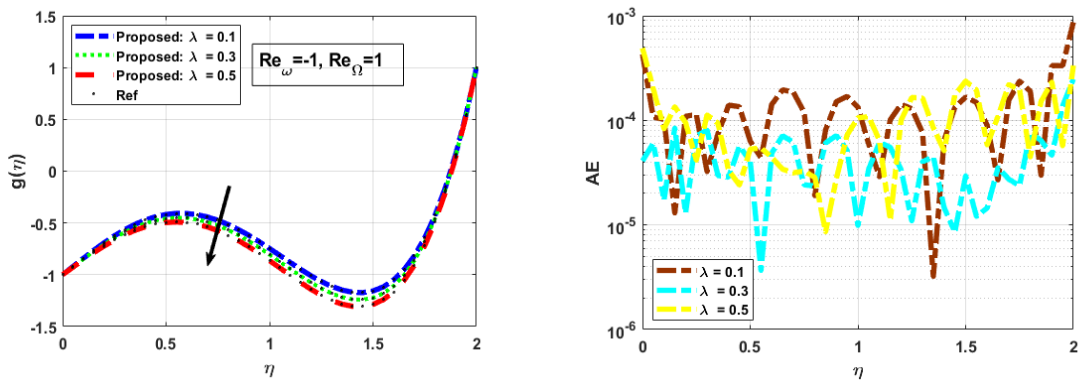


Fig. 17. (a) Variation in  $\lambda$  vs  $g(\eta)$  (b) AE for  $\lambda$ .

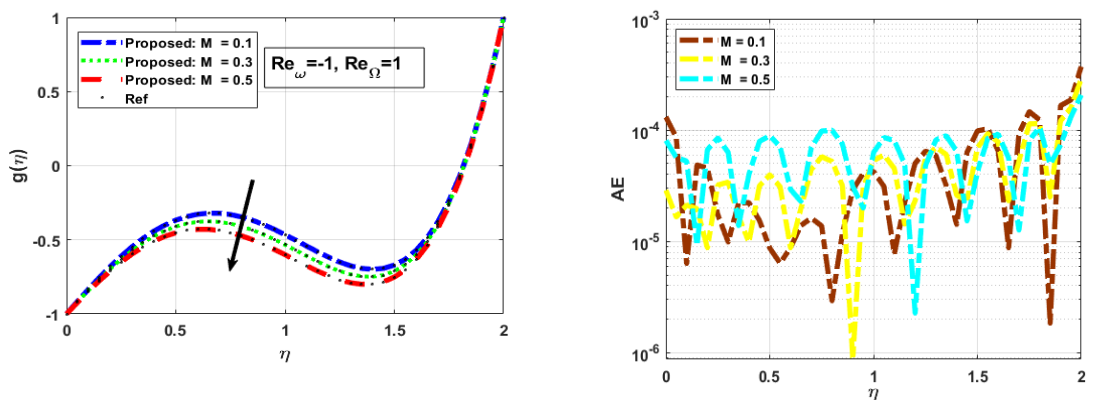


Fig. 18. (a) Variation in  $M$  vs  $g(\eta)$  (b) AE for  $M$ .





**(c) Biomedical Fluidic Devices:**

Scenario (iii) Cone and Disk Gyration in Same Direction: In biomedical engineering applications, where precise control of fluid flow is essential in devices like microfluidic systems for drug delivery or diagnostic assays, understanding the retardation in transverse velocity is crucial. This knowledge aids in designing fluidic devices that accurately manipulate fluids for biomedical purposes.

**(d) Fluidic Systems for Lab-on-a-Chip Technology:**

Scenario (iv) Cone and Disk Gyration in Opposite Directions: Lab-on-a-chip technology, used for various analytical and diagnostic purposes, often employs microfluidic systems. The retardation in transverse velocity influenced by magnetic and rheological factors can impact the accuracy and efficiency of these fluidic systems, requiring careful consideration in their design. In each scenario, the retardation in transverse velocity due to the magnetic and Jeffrey fluid factors has specific consequences for the performance of engineering systems. These applications span a range of fields, emphasizing the broad relevance of understanding and incorporating these factors in the design and optimization of diverse engineering processes and devices.

**5. Conclusions**

In this study, the Jeffrey fluid flow was taken through the gap between cone and disk with the influence of Boungiorno model. The flow model was converted to a set of nonlinear ODEs and then neuro computational technique was employed to find its solution. Four different scenarios for fluid flow through the gap of disk and cone have been examined. An Artificial Neural Network (ANN) was employed to effectively manipulate and enhance fluid flow behavior within the given flow problem. The results of our study underscored the effectiveness of this innovative approach, highlighting its potential to revolutionize fluid flow control across a wide spectrum of engineering applications. The design methodology for tackling various aspects of the fluid problem follows a structured sequence, which involves training, testing, and validation utilizing a reference dataset. After a detailed analysis of the problem, the following key points have been identified and recovered:

- Studying the flow behavior of Jeffrey nanofluids through the cone-disk gap is important for understanding their heat transfer characteristics in thermal applications. By examining factors such as nanoparticle concentration, viscoelastic additives, cone angle, and gap size, researchers can optimize the design of cone-disk systems to enhance heat transfer efficiency.
- The flow model exhibits outstanding performance during training, testing, and validation across momentum, energy, and concentration equations. These results consistently show a close alignment and agreement among these equations on average  $10^{-8}$ .
- Absolute error between targeted data and reference falls between the range of  $10^{-4}$  to  $10^{-5}$ , demonstrating the exceptional accuracy performance of LMS-NNA.
- In all four scenarios (i) static cone and gyrating disk  $Re_\omega = 0, Re_\Omega = 1$ , (ii) static disk and gyrating cone  $Re_\omega = 1, Re_\Omega = 0$ , (iii) cone and disk move in similar direction  $Re_\omega = 1, Re_\Omega = 2$ , (iv) cone and disk move in reverse directions  $Re_\omega = -1, Re_\Omega = 1$ , it has noticed that transverse velocity distribution has declined with augmentation in magnetic and Jeffrey fluid factors by keeping all the other parameters as fixed.
- It is evident that the optimal validation performance  $2.8227 \times 10^{-9}$  has been achieved at epoch 1000 for the transverse velocity of the HIE-PNF-NFDDT fluid model about fluid flow through the space between cone and gap, with cone and disk gyrating in opposite directions and encompassing MSE results, transition states, error histograms, fitting curves, and regression analysis.
- Computational values for various factors in the ANN models have been evaluated including distinct computational values for MSE, performance, gradient, and mu, across different epochs (1000, 597, 497, 909, 1000, 1000, 1000, 1000) for all the four scenarios of disk cone devices.
- The gradient values are found for all the eight cases which fall as  $2.02 \times 10^{-7}$ ,  $9.87 \times 10^{-8}$ ,  $1.0 \times 10^{-7}$ ,  $9.97 \times 10^{-8}$ ,  $2.70 \times 10^{-6}$ ,  $6.13 \times 10^{-7}$ ,  $5.66 \times 10^{-7}$  and  $2.2 \times 10^{-6}$ .
- The maximum error for training, testing and validation of the proposed model are achieved at  $4.00 \times 10^{-5}$ ,  $1.00 \times 10^{-5}$ ,  $1.00 \times 10^{-4}$ ,  $1.5 \times 10^{-5}$ ,  $0.5 \times 10^{-4}$ ,  $2.5 \times 10^{-5}$ ,  $2.5 \times 10^{-4}$  and  $1.00 \times 10^{-4}$ .

**Author Contributions**

A.S. Alnahdi, T. Gul, Z. Khan: Solution and writing manuscript; T. Gul, H. Ahmad: Software; A.S. Alnahdi, T. Gul, Z. Khan, H. Ahmad: Validation. The manuscript was written through the contribution of all authors. All authors discussed the results, reviewed, and approved the final version of the manuscript.

**Acknowledgments**

The authors extend their appreciation to the Deanship of Scientific Research at Imam Mohammad Ibn Saud Islamic University (IMSIU) for funding this work; (grant number IMSIU-RP23059).

**Conflict of Interest**

The authors declared no potential conflicts of interest concerning the research, authorship, and publication of this article.

**Funding**

This work was supported and funded by the Deanship of Scientific Research at Imam Mohammad Ibn Saud Islamic University (IMSIU) (grant number IMSIU-RP23059).

**Data Availability Statements**

The datasets generated and/or analyzed during the current study are available from the corresponding author on reasonable request.




## References


- [1] Wang, F., Rani, S.P., Sarada, K., Gowda, R.P., Zahran, H.Y., Mahmoud, E.E., The effects of nanoparticle aggregation and radiation on the flow of nanofluid between the gap of a disk and cone, *Case Studies in Thermal Engineering*, 33, 2022, 101930.
- [2] Moatimid, G.M., Mohamed, M.A., Elagamy, K., A Casson nanofluid flow within the conical gap between rotating surfaces of a cone and a horizontal disc, *Scientific Reports*, 12(1), 2022, 11275.
- [3] Sheikholeslami, M., Numerical investigation of solar system equipped with innovative turbulator and hybrid nanofluid, *Solar Energy Materials and Solar Cells*, 243, 2022, 111786.
- [4] Turkyilmazoglu, M., On the fluid flow and heat transfer between a cone and a disk both stationary or rotating, *Mathematics and Computers in Simulation*, 177, 2020, 329-340.
- [5] Srilatha, P., Remidi, S., Nagapavani, M., Singh, H., Prasannakumara, B.C., Heat and mass transfer analysis of a fluid flow across the conical gap of a cone-disk apparatus under the thermophoretic particles motion, *Energies*, 16(2), 2023, 952.
- [6] Moatimid, G.M., Mohamed, M.A., Elagamy, K., A Casson nanofluid flow within the conical gap between rotating surfaces of a cone and a horizontal disc, *Scientific Reports*, 12(1), 2022, 11275.
- [7] Shevchuk, I.V., An improved asymptotic expansion method for fluid flow and convective heat transfer in cone-and-disk geometries with rotating cone, *Physics of Fluids*, 35(4), 2023, 043603.
- [8] Sheikholeslami, M., Numerical investigation for concentrated photovoltaic solar system in existence of paraffin equipped with MWCNT nanoparticles, *Sustainable Cities and Society*, 99, 2023, 104901.
- [9] Mandal, A., Mondal, H., Tripathi, R., Activity of motile microorganism in bioconvective nanofluid flow with Arrhenius activation energy, *Journal of Thermal Analysis and Calorimetry*, 148(17), 2023, 9113-9130.
- [10] Nazeer, M., Hussain, F., Ahmad, M.O., Saeed, S., Khan, M.I., Kadry, S., Chu, Y.M., Multi-phase flow of Jeffrey Fluid bounded within magnetized horizontal surface, *Surfaces and Interfaces*, 22, 2021, 100846.
- [11] Rehman, K.U., Shatanawi, W., Al-Mdallal, Q.M., A comparative remark on heat transfer in thermally stratified MHD Jeffrey fluid flow with thermal radiations subject to cylindrical/plane surfaces, *Case Studies in Thermal Engineering*, 32, 2022, 101913.
- [12] Sharma, B.K., Kumar, A., Gandhi, R., Bhatti, M.M., Exponential space and thermal-dependent heat source effects on electro-magneto-hydrodynamic Jeffrey fluid flow over a vertical stretching surface, *International Journal of Modern Physics B*, 36(30), 2022, 2250220.
- [13] Agarwal, K., Baghel, R.S., Parmar, A., Dadheech, A., Jeffery Slip Fluid Flow with the Magnetic Dipole Effect Over a Melting or Permeable Linearly Stretching Sheet, *International Journal of Applied and Computational Mathematics*, 10(1), 2024, 1-17.
- [14] Agarwal, V., Singh, B., Nisar, K.S., Numerical analysis of heat transfer in magnetohydrodynamic micropolar jeffery fluid flow through porous medium over a stretching sheet with thermal radiation, *Journal of Thermal Analysis and Calorimetry*, 147(17), 2022, 9829-9851.
- [15] Benal, S.S., Tawade, J.V., Biradar, M.M., Allasi, H.L., Effects of the magnetohydrodynamic flow within the boundary layer of a jeffery fluid in a porous medium over a shrinking/stretching sheet, *Mathematical Problems in Engineering*, 2022, 2022, 7326504.
- [16] Awais, M., Rehman, H., Raja, M.A.Z., Awan, S.E., Ali, A., Shoaib, M., Malik, M.Y., Hall effect on MHD Jeffrey fluid flow with Cattaneo-Christov heat flux model: An application of stochastic neural computing, *Complex & Intelligent Systems*, 8(6), 2022, 5177-5201.
- [17] Nazeer, M., Hussain, F., Khan, M.I., Khalid, K., Theoretical analysis of electrical double layer effects on the multiphase flow of Jeffrey fluid through a divergent channel with lubricated walls, *Waves in Random and Complex Media*, 2022, DOI: 10.1080/17455030.2022.2126025.
- [18] Verma, L., Meher, R., Effect of heat transfer on Jeffery-Hamel Cu/Ag-water nanofluid flow with uncertain volume fraction using the double parametric fuzzy homotopy analysis method, *The European Physical Journal Plus*, 137(3), 2022, 372.
- [19] Kukreja, H., Bharath, N., Siddesh, C.S., Kuldeep, S., An introduction to artificial neural network, *International Journal of Advance Research and Innovative Ideas in Education*, 1, 2016, 27-30.
- [20] Morimoto, M., Fukami, K., Zhang, K., Fukagata, K., Generalization techniques of neural networks for fluid flow estimation, *Neural Computing and Applications*, 34, 2022, 3647-3669.
- [21] Li, A., Yuen, A.C.Y., Wang, W., Chen, T.B.Y., Lai, C.S., Yang, W., Wu, W., Chan, Q.N., Kook, S., Yeoh, G.H., Integration of computational fluid dynamics and artificial neural network for optimization design of battery thermal management system, *Batteries*, 8(7), 2022, 69.
- [22] Affonso, R.R., Dam, R.S., Salgado, W.L., da Silva, A.X., Salgado, C.M., Flow regime and volume fraction identification using nuclear techniques, artificial neural networks and computational fluid dynamics, *Applied Radiation and Isotopes*, 159, 2020, 109103.
- [23] Samanta, A., Mondal, H., Prediction model based on artificial neural network and bivariate spectral quasi-linearization method for compressible turbulent boundary-layer flow over a smooth flat surface, *Physics of Fluids*, 35(12), 2023, 125148.
- [24] Mishra, S., Mondal, H., A Neuro-computational Proposal for the ZrO<sub>2</sub>-Fe<sub>3</sub>O<sub>4</sub> Nanoparticles in the Engine Oil-based Hybrid Nanofluid, *BioNanoScience*, 2023, DOI: 10.1007/s12668-023-01282-z.
- [25] Raja, M.A.Z., Shoaib, M., Tabassum, R., Khan, N.M., Kehili, S., Bafakeeh, O.T., Stochastic numerical computing for entropy optimized of Darcy-Forchheimer nanofluid flow: Levenberg Marquardt Algorithm, *Chemical Physics Letters*, 807, 2022, 140070.
- [26] Rehman, K.U., Shatanawi, W., Çolak, A.B., Computational Analysis on Magnetized and Non-Magnetized Boundary Layer Flow of Casson Fluid Past a Cylindrical Surface by Using Artificial Neural Networking, *Mathematics*, 11(2), 2023, 326.
- [27] Aljohani, J.L., Alaidarous, E.S., Raja, M.A.Z., Alhothuali, M.S., Shoaib, M., Backpropagation of Levenberg Marquardt artificial neural networks for wire coating analysis in the bath of Sisko fluid, *Ain Shams Engineering Journal*, 12(4), 2021, 4133-4143.
- [28] Sulaiman, M., Khan, N.A., Alshammari, F.S., Laouini, G., Performance of heat transfer in micropolar fluid with isothermal and isoflux boundary conditions using supervised neural networks, *Mathematics*, 11(5), 2023, 1173.
- [29] Sharma, B.K., Khanduri, U., Mishra, N.K., Mekheimer, K.S., Combined effect of thermophoresis and Brownian motion on MHD mixed convective flow over an inclined stretching surface with radiation and chemical reaction, *International Journal of Modern Physics B*, 37(10), 2023, 2350095.
- [30] Rashid, A., Dawar, A., Ayaz, M., Islam, S., Galal, A.M., Gul, H., Homotopic solution of the chemically reactive magnetohydrodynamic flow of a hybrid nanofluid over a rotating disk with Brownian motion and thermophoresis effects, *ZAMM-Journal of Applied Mathematics and Mechanics/Zeitschrift für Angewandte Mathematik und Mechanik*, 103, 2023, e202200262.
- [31] Khan, A., Iqbal, Z., Ahammad, N.A., Sidi, M.O., Elattar, S., Awad, S., Eldin, S.M., Bioconvection Maxwell nanofluid flow over a stretching cylinder influenced by chemically reactive activation energy surrounded by a permeable medium, *Frontiers in Physics*, 10, 2023, 1348.
- [32] Magodora, M., Mondal, H., Motsa, S., Sibanda, P., Numerical studies on gold-water nanofluid flow with activation energy Past A rotating disk, *International Journal of Applied and Computational Mathematics*, 8(1), 2022, 41.
- [33] Sheikholeslami, M., New computational approach for exergy and entropy analysis of nanofluid under the impact of Lorentz force through a porous media, *Computer Methods in Applied Mechanics and Engineering*, 344, 2019, 319-333.
- [34] Almakki, M., Mondal, H., Mburu, Z., Sibanda, P., Entropy generation in double diffusive convective magnetic nanofluid flow in rotating sphere with viscous dissipation, *Journal of Nanofluids*, 11(3), 2022, 360-372.
- [35] Sheikholeslami, M., Numerical approach for MHD Al<sub>2</sub>O<sub>3</sub>-water nanofluid transportation inside a permeable medium using innovative computer method, *Computer Methods in Applied Mechanics and Engineering*, 344, 2019, 306-318.
- [36] Felicita, A., Venkatesh, P., Gireesha, B.J., Krishnamurthy, M.R., Slip and convective flow of Williamson nanofluid influenced by Brownian motion and thermophoresis mechanism in a horizontal microchannel, *Proceedings of the Institution of Mechanical Engineers, Part N: Journal of Nanomaterials, Nanoengineering and Nanosystems*, 2023, DOI: 10.1177/23977914231177340.
- [37] Ibrahim, S.M., Kumar, P.V., Lorenzini, G., Influence of Thermophoresis and Brownian Motion of Nanoparticles on Radiative Chemically-Reacting MHD Hiemenz Flow over a Nonlinear Stretching Sheet with Heat Generation, *Fluid Dynamics & Materials Processing*, 19(4), 2023, 855-868.
- [38] Almeida, F., Gireesha, B.J., Venkatesh, P., Magnetohydrodynamic flow of a micropolar nanofluid in association with Brownian motion and thermophoresis: Irreversibility analysis, *Heat Transfer*, 52(2), 2023, 2032-2055.
- [39] Khan, A., Gul, T., Ali, I., Khalifa, H.A.E.W., Muhammad, T., Alghamdi, W., Shaaban, A.A., Thermal examination for double diffusive MHD Jeffrey fluid flow through the space of disc and cone apparatus subject to impact of multiple rotations, *International Journal of Heat and Fluid Flow*, 106, 2024, 109295.
- [40] Gul, T., Ahmed, Z., Jawad, M., Saeed, A., Alghamdi, W., Bio-convectational nanofluid flow due to the thermophoresis and gyrotactic microorganism between the gap of a disk and cone, *Brazilian Journal of Physics*, 51(3), 2021, 687-697.





- [41] Farooq, U., Waqas, H., Fatima, N., Imran, M., Noreen, S., Bariq, A., Galal, A.M., Computational framework of cobalt ferrite and silver-based hybrid nanofluid over a rotating disk and cone: a comparative study, *Scientific Reports*, 13(1), 2023, 5369.
- [42] Ahmadi, M.H., Mohseni-Gharyehsafa, B., Ghazvini, M., Goodarzi, M., Jilte, R.D., Kumar, R., Comparing various machine learning approaches in modeling the dynamic viscosity of CuO/water nanofluid, *Journal of Thermal Analysis and Calorimetry*, 139, 2020, 2585-2599.
- [43] Ali, A., Ahammad, N.A., Tag-Eldin, E., Gamaoun, F., Daradkeh, Y.I., Yassen, M.F., MHD Williamson nanofluid flow in the rheology of thermal radiation, Joule heating, and chemical reaction using the Levenberg-Marquardt neural network algorithm, *Frontiers in Energy Research*, 10, 2022, 1175.
- [44] Liu, T., Li, Y., Jing, Q., Xie, Y., Zhang, D., Supervised learning method for the physical field reconstruction in a nanofluid heat transfer problem, *International Journal of Heat and Mass Transfer*, 165, 2021, 120684.
- [45] Raja, M.A.Z., Shoaib, M., Khan, Z., Zuhra, S., Saleel, C.A., Nisar, K.S., Khan, I., Supervised neural networks learning algorithm for three dimensional hybrid nanofluid flow with radiative heat and mass fluxes, *Ain Shams Engineering Journal*, 13(2), 2022, 101573.
- [46] Mishra, S.R., Baag, S., Mohapatra, D.K., Chemical reaction and Soret effects on hydromagnetic micropolar fluid along a stretching sheet, *Engineering Science and Technology, an International Journal*, 19(4), 2016, 1919-1928.
- [47] Öcal, S., Gökçek, M., Çolak, A.B., Korkanç, M., A comprehensive and comparative experimental analysis on thermal conductivity of TiO<sub>2</sub>-CaCO<sub>3</sub>/Water hybrid nanofluid: Proposing new correlation and artificial neural network optimization, *Heat Transfer Research*, 52(17), 2021, 55-79.

## ORCID iD

Abeer S. Alnahdi  <https://orcid.org/0000-0002-8027-2529>

Zeeshan Khan  <https://orcid.org/0000-0001-8595-1419>

Taza Gul  <https://orcid.org/0000-0003-1376-8345>

Hijaz Ahmad  <https://orcid.org/0000-0002-5438-5407>



© 2024 Shahid Chamran University of Ahvaz, Ahvaz, Iran. This article is an open access article distributed under the terms and conditions of the Creative Commons Attribution-NonCommercial 4.0 International (CC BY-NC 4.0 license) (<http://creativecommons.org/licenses/by-nc/4.0/>).

**How to cite this article:** Alnahdi A.S., Khan Z., Gul T., Ahmad H. The Flow of Jeffrey Nanofluid through Cone-Disk Gap for Thermal Applications using Artificial Neural Networks, *J. Appl. Comput. Mech.*, xx(x), 2024, 1-19.  
<https://doi.org/10.22055/jacm.2024.45278.4345>

**Publisher's Note** Shahid Chamran University of Ahvaz remains neutral with regard to jurisdictional claims in published maps and institutional affiliations.

